ISSN 2587-1366

TUJE

TURKISH JOURNAL OF ENGINEERING

VOLUME 2 ISSUE 1 JANUARY 2018

TURKISH JOURNAL OF ENGINEERING (TUJE)

Turkish Journal of Engineering (TUJE) is a multi-disciplinary journal. The Turkish Journal of Engineering (TUJE) publishes the articles in English and is being published 3 times (January, May, September) a year. The Journal is a multidisciplinary journal and covers all fields of basic science and engineering. It is the main purpose of the Journal that to convey the latest development on the science and technology towards the related scientists and to the readers. The Journal is also involved in both experimental and theoretical studies on the subject area of basic science and engineering. Submission of an article implies that the work described has not been published previously and it is not under consideration for publication elsewhere. The copyright release form must be signed by the corresponding author on behalf of all authors. All the responsibilities for the article belongs to the authors. The publications of papers are selected through double peer reviewed to ensure originality, relevance and readability.

AIM AND SCOPE

The Journal publishes both experimental and theoretical studies which are reviewed by at least two scientists and researchers for the subject area of basic science and engineering in the fields listed below:

Aerospace Engineering
Environmental Engineering
Civil Engineering
Geomatic Engineering
Mechanical Engineering
Geology Science and Engineering
Mining Engineering
Chemical Engineering
Metallurgical and Materials Engineering
Electrical and Electronics Engineering
Mathematical Applications in Engineering
Computer Engineering
Food Engineering

PEER REVIEW PROCESS

All submissions will be scanned by iThenticate® to prevent plagiarism. Author(s) of the present study and the article about the ethical responsibilities that fit PUBLICATION ETHICS agree. Each author is responsible for the content of the article. Articles submitted for publication are priorly controlled via iThenticate ® (Professional Plagiarism Prevention) program. If articles that are controlled by iThenticate® program identified as plagiarism or self-plagiarism with more than 25% manuscript will return to the author for appropriate citation and correction. All submitted manuscripts are read by the editorial staff. To save time for authors and peer-reviewers, only those papers that seem most likely to meet our editorial criteria are sent for formal review. Reviewer selection is critical to the publication process, and we base our choice on many factors, including expertise, reputation, specific recommendations and our own previous experience of a reviewer's characteristics. For instance, we avoid using people who are slow, careless or do not provide reasoning for their views, whether harsh or lenient. All submissions will be double blind peer reviewed. All papers are expected to have original content. They should not have been previously published and it should not be under review. Prior to the sending out to referees, editors check that the paper aim and scope of the journal. The journal seeks minimum three independent referees. All submissions are subject to a double blind peer review; if two of referees gives a negative feedback on a paper, the paper is being rejected. If two of referees gives a positive feedback on a paper and one referee negative, the editor can decide whether accept or reject. All submitted papers and referee reports are archived by journal Submissions whether they are published or not are not returned. Authors who want to give up publishing their paper in TUJE after the submission have to apply to the editorial board in written. Authors are responsible from the writing quality of their papers. TUJE journal will not pay any copyright fee to authors. A signed Copyright Assignment Form has to be submitted together with the paper.

PUBLICATION ETHICS

Our publication ethics and publication malpractice statement is mainly based on the Code of Conduct and Best-Practice Guidelines for Journal Editors. Committee on Publication Ethics (COPE). (2011, March 7). Code of Conduct and Best-Practice Guidelines for Journal Editors. Retrieved from http://publicationethics.org/files/Code%20of%20Conduct_2.pdf

PUBLICATION FREQUENCY

The TUJE accepts the articles in English and is being published 3 times. January, May, September a year.

CORRESPONDENCE ADDRESS

Journal Contact: tuje@mersin.edu.tr

CONTENTS

Volume 2 – Issue 1

ARTICLES

CHARACTERIZATION OF HYDROTHERMALLY SYNTHESISED HYDROXYAPATITE BIOCERAMIC
Canan Aksu Canbay, Himdad İbrahim Mustafa and İskender Özkul **1**

AGING EFFECTS ON TRANSFORMATION TEMPERATURES AND ENTHALPIES FOR TiNi ALLOY
Canan Aksu Canbay and İskender Özkul **7**

THE EFFECT OF SODIUM CARBONATE ON ELEVATED TEMPERATURE RESISTANCE OF CEMENT MORTARS CONTAINING NATURAL ZEOLITE
Cahit Bilim **12**

LIGHTWEIGHT FOAM IMPACT ATTENUATOR DESIGN FOR FORMULA SAE CAR
Emre İsa Albak, Erol Solmaz, Necmettin Kaya and Ferruh Öztürk **17**

GALVANIC CORROSION OF ZINC ANODE AND COPPER CATHODE CELL
Nurettin Çek **22**

APPLICABILITY OF SOLAR AND WIND ENERGY TECHNOLOGIES FOR A NON-RESIDENTIAL BUILDING
Burhan Bayhan and Gökhan Arslan **27**

MEASURES TO BE DETERMINED AND RECEIVED IN UNIVERSITIES OF OCCUPATIONAL HEALTH AND SAFETY RISKS
Mehmet Zile **35**

Turkish Journal of Engineering

Turkish Journal of Engineering (TUJE)
Vol. 2, Issue 1, pp. 1-6, January 2018
ISSN 2587-1366, Turkey
DOI: 10.31127/tuje.327822
Research Article

CHARACTERIZATION OF HYDROTHERMALLY SYNTHESISED HYDROXYAPATITE BIOCERAMIC

Canan Aksu Canbay *[1], Himdad İbrahim Mustafa [2] and İskender Özkul [3]

[1] Fırat University, Faculty of Science, Department of Physics, Elazığ, Turkey
ORCID ID 0000-0002-5151-4576
caksu@firat.edu.tr

[2] Fırat University, Faculty of Science, Department of Physics, Elazığ, Turkey
ORCID ID 0000-0001-5174-2555
himdadibrahim88@gmail.com

[3] Mersin University, Engineering Faculty, Department of Mechanical Engineering, Mersin, Turkey
ORCID ID 0000-0003-4255-0564
iskender@mersin.edu.tr

* Corresponding Author
Received: 11/07/2017 Accepted: 14/09/2017

ABSTRACT
In this study, hydroxyapatite (HAP) was synthesized by hydrothermal method. The structural analysis, thermal analysis and electrical characteristics of HAP sample have been investigated. The structural analysis was performed to determine the crystal structure and to observe the surface morphology of the sample. The thermal analysis was made from room temperature to 925 ˚C, to determine the mass loss according to temperature and phase transitions or decomposition in the sample and also TG-DTA analysis was done to determine the thermal stability. The compositional analysis was done by EDX. I-V analysis was made to calculate the electrical conductivity value of the sample and electrical conductivity of the sample was obtained to be$1.2x10^{-10}$ S/cm.

Keywords: *Hydroxyapatite (HAP), Hydrothermal Method, Electrical Conductivity*

1. INTRODUCTION

With the developing technology, the depth of material properties can be reached. In this respect, it is possible to find a faster solution to the needs of mankind. Nanotechnology is a new trend in today's technology. In the transition from macro structure to micro structure, unanswered questions began to be answered gradually. Materials that have been obtained in very small sizes have been a source of inspiration for a lot of work such as nanotube, nanowire etc. At the same time, thanks to the material structure, it has been well understood how to synthesize the materials as well as how the existing materials can be developed. Developments in bio ceramic materials, which have a different place in materials, are important for human anatomy (Brown *et al.*, 1994; Gümüşderelioğlu, 2002; Orlovskii *et al.*, 2002). Today, the issue of biocompatibility of materials becomes increasingly important (Pasinli, 2004). Determination should be made as to the purpose of use in the between materials with direct contact with blood and other materials, and this biocompatibility should be assessed within its own environment (Gümüşderelioğlu, 2002; Park *et al.*, 2002). Semi-biological body parts used in medical interventions that are necessary after the diseases or accidents must meet the requirements as mechanical properties at the same time.

Hydroxyapatite (HAP) in these materials constitutes the main mineral components of materials such as teeth, bones. Hydroxyapatite is a biologically dynamic calcium phosphate ceramic that can be used in surgical operations. Although HAP powder bioactivity has a large hold on bone development along its surface, it is insufficient to withstand severe load in terms of mechanical properties. Hydroxyapatite is a biological apatite as it is in the living bone component. The biological apatite weighs 70% of the bone (Singh *et al.*, 2014). Hydroxyapatite is a biologically dynamic calcium phosphate ceramic that can be used in surgical operations. Although HAP powder bioactivity has a large hold on bone development along its surface, it is insufficient to withstand severe load in terms of mechanical properties (Singh and Sidhu, 2014). Hydroxyapatite is a biological apatite as it is in the living bone component. Almost 70% of the bone forms biological apatite (Singh and Sidhu, 2014). Besides, the HAP in bone is found with other ions such as impure fluoride, magnesium and sodium (Sadat-Shojai *et al.*, 2013). The HAP is chemically represented as $Ca_{10}(PO_4)_6(OH)_2$ and its crystal structure is shown in Fig. 1.

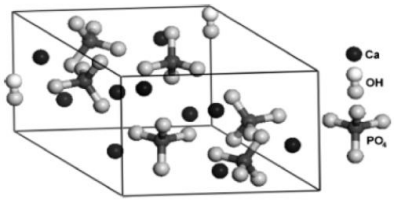

Fig. 1. Crystal structure of hydroxyapatite (Zhang, 2007).

The HAP materials can be synthesized in many different methods (Sadat-Shojai *et al.*, 2013) and uses. HAP also can be coated by stronger materials lie zirconium and aluminum oxide to provide high mechanical properties. That uses make more successful operations in clinical practice (Hench *et al.*, 1993; Brown and Constantz, 1994; Orlovskii *et al.*, 2002). In our study we have synthesized Hydroxyapatite bio ceramic material. The developed HAP characterization has been made and results are discussed.

2. MATERIALS AND METHOD

The nanostructured hydroxyapatite bio ceramic (10mmol) calcium nitrate tetrahydrate $Ca(NO_3)_2\,4H_2O$ is dissolved in 30mL distilled water than solution mixed by magnetic stirrer for 30 mins. at 60°C, and 6mmol ammonium hydrogen phosphate $(NH_4)_2HPO_4$ is dissolved in 30mL distilled water, was added to the solution. Both solutions separately sonicated for 10 min. After the addition of 40 mg of cetyltrimethyl ammonium bromide to the solution and sonicated 60 mins., the ratio of Ca/P in the solution was maintained 1.67. Also, put hydrothermal 24 hours at 180°C and at 140°C in 100 mL water in an autoclave. After 24 hours filtering, the solution cleaned then dried in the oven. Then calcinated at 700°C in a furnace evaporate the nitrates and hydrates from the structure. In addition, the detailed sample preparation procedure and the crystalline phases of synthesised nanostructured hydroxyapatite bio ceramic were determined by X-ray diffraction (XRD) analysis on the Rigaku RadB-DMAX II diffractometer with CuKα radiation at room temperature. Morphological features of hydroxyapatite bio ceramic coatings were observed by scanning electron microscopy (SEM) executed on a scanning electron microscope JEOL-7001 and EDX performed on Energy Dispersive X-ray analysis JEOL-7001. Fourier transform infrared (FTIR) spectroscopy was taken (Thermo scientific Nicole IS 5) and we to used Keithley 4200 semiconductor characterization system for current-voltage (I-V) analysis. The weight loss measurements made by thermogravimetric analysis (TGA) and the phase transitions occurred in the sample was analysed by differential thermal analysis (DTA) by SHIMADZU DTG-60AH equipment.

2.1. Results and Discussions

Analyzes and results have been individually assessed within themselves.

2.1.1. X-Ray Analysis

XRD spectra of the HAP taken within a 2θ range of 20-80° are shown in Fig. 2. The mean crystallite size D of the sample was computed by analyzing the XRD data using the Debye - Scherrer formula:

$$\mathbf{D} = \frac{\mathbf{k\lambda}}{\boldsymbol{\beta}\,\mathbf{cos}\,\boldsymbol{\theta}} \qquad (1)$$

where D represents average crystalline size, λ is the wavelength of X-ray (0.1540559 nm), θ is the peak angle of diffraction degree (Bragg's angle) and β is the full width of the peak at the half-maximum intensity in radian (FWHM), also Scherrer constant defined as the crystallite shape and is around equal to 0.9. Sharp peaks appeared in the XRD patterns of the calcined HAP powders revealed good crystallinity. The characteristic peak of the sample appears at 2θ = 29.08, corresponding to (210) plane of

HAP, which confirms the presence of HAP crystallite. The average crystalline size of all samples scaffold were estimated using Debye-Scherer equation confirming the nanostructure of the nano-composite and was found to be 12.2 nm, this range confirms that all the studied composites are nanostructured materials (Padiyan *et al.*, 2003; Badran *et al.*, 2017).

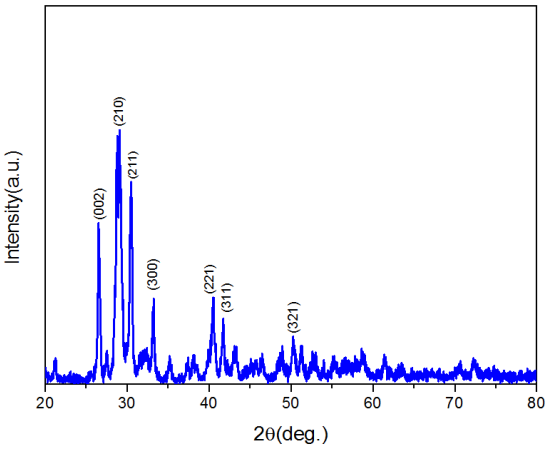

Fig. 2. XRD patterns of HAP powder in the sample

2.1.2. FTIR Analysis

FTIR is a way utilised for chemical identification, principled on the actuality that the selective absorption of material happens in the infrared domain. The molecule of chemical substance vibrates in numerous modes later absorption of infrared giving fourier transform infrared spectroscopy absorption spectrum, above broad wavelength scope. FTIR analyses helped us to reveal the chemical bonding characteristics with the powder samples. FTIR spectra of the HAP are shown in Fig. 3. All the bands corresponding to HAP structure were observed in FTIR spectrums. The observed bands correspond to the bands of hydroxyl and absorbed water phosphate species (Sato *et al.*, 2006). Characteristic bands for phosphate stretching vibrations and phosphate banding appeared in the region (950 cm^{-1} -1250 cm^{-1}). The bands at (903 cm^{-1}–962 cm^{-1}) correspond to ν_1 stretching mode of PO_4^{3-} group while the bands at (1032cm^{-1}–1092 cm^{-1}) correspond to ν_3 stretching mode(Stanić *et al.*, 2010; Zhang *et al.*, 2010). PO_4 bands at (1091cm^{-1}–962 cm^{-1}) confirm the formation of HAP structure. The most intense peak among the phosphate group was observed in the region of ~720cm^{-1} (Sato *et al.*, 2006; Al-Hazmi, 2016). The obtained all FTIR bands are in good agreement by the bands of HAP (Sato *et al.*, 2006). The appearance of the sharp peaks associated with the stretching vibration in investigated samples indicates to the formation of crystalline HAP.

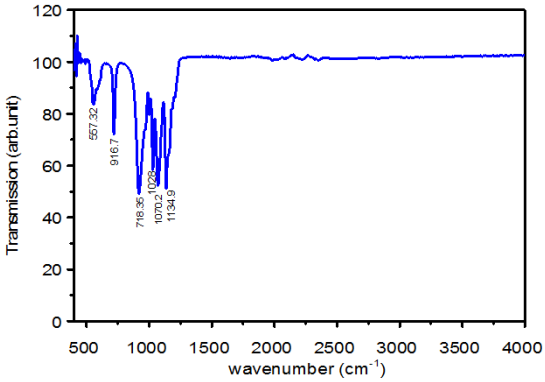

Fig. 3. FTIR spectra of HAP in the sample

2.1.3.SEM and EDX Analysis

Scanning electron microscopy instrument has been used to obtain the morphology of HAP. The SEM images of the HAP in the range microparticle are shown in Figs. 4-7. The morphology of HAP sample exhibits plate-like structure with a smooth surface 6000X magnification. The elemental analysis with the HAP sample was performed by X-ray Energy Dispersive spectroscopy (EDS). The phosphorus, calcium and oxygen were observed in EDS spectra of report which presented in Table 1. The elemental composition and homogeneity of particles have major effects on biocompatibility and bioactivity properties of bio ceramic materials. To know the inter relationship between materials properties, the composition of the material should be known. This technique was utilised to analyses of HAP specimen. Organic reactions of a HAP sample are powerfully depending on its chemical composition, energy dispersive spectroscopy (EDS), result uncovers that HAP specimen contains Ca, P and O. The best Ca/P ratio for synthesised specimen was observed to be 1.65, which is somewhat smaller than 1.67 theoretical worth and the similar was usually reported (Jagadale *et al.*, 2016).

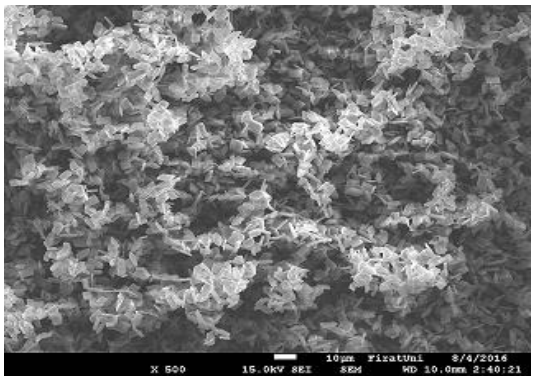

Fig. 4. SEM (10µm) of HAP in the sample at 500x magnification.

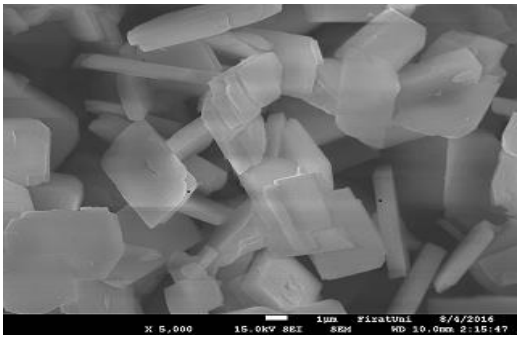

Fig. 5. SEM (1µm) of HAP sample at 6000x magnification.

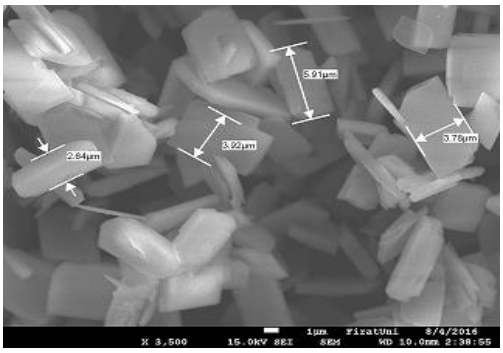

Fig. 6. SEM (1µm) of HAP in the sample at 3500x magnification

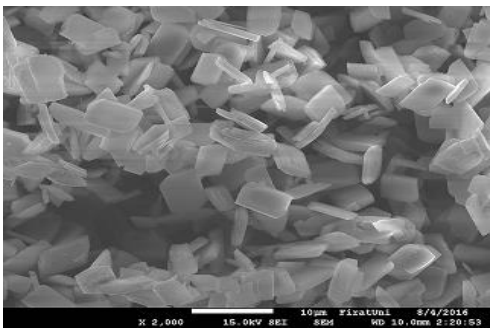

Fig. 7. SEM (10µm) of HAP in the sample at 2000x magnification

Table 1. This is the example for table formatting

Element	Weight%	Atomic%
O	11.49	22.63
P	33.66	34.24
Ca	54.85	43.12

2.1.4. TGA/DTA Analysis

Thermogravimetric analysis (TGA) and Differential thermal analysis (DTA) for hydroxyapatite sample was made from room temperature to 925°C. Thermal stability of HAP sample was examined by thermal decomposition of the powder. The TGA/DTA results are shown in Fig. 8. The TGA (thermogravimetric analysis) demonstrates total weight loss is 8.583% in the temperature range from room temperature to 925°C that the decomposition of HAP sample due to evaporation of physically adsorbed water is given in Fig. 9. DTA (differential thermal analysis) curve shows that thermal decomposition of HAP sample at 290.76°C with an endothermic peak and this peak is alone due to degradation of residual water from the sample shown in Fig. 10. The result of thermal decomposition is useful for optimization of conditions to obtain monophasic biomaterial.

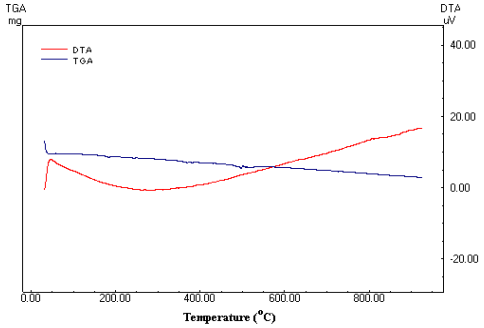

Fig. 8. TG/DTA curves of the sample

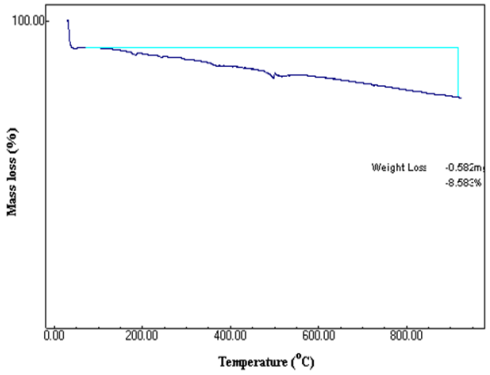

Fig. 9. TG curve of the sample

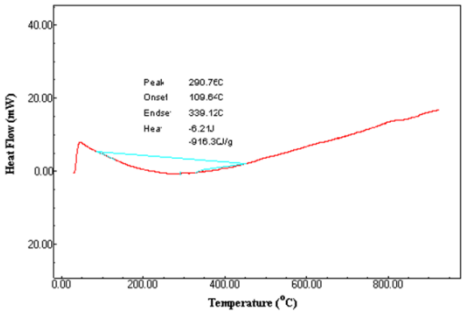

Fig. 10. DTA curve of the sample

2.1.5. I-V Characterization

In I-V characterization the current slope of the sample according to the voltage value was provided. So the graph of current versus voltage value can be drawn. In this graph, the resistivity of the sample was found. From this point, the slope (3.9756×10^{-10}S) of the sample as seen in

Fig. 11 was found, and then the slope of the graph to calculate the electrical conductivity was used by the help of the following equation:

$$\boldsymbol{\sigma = \frac{I}{V} . \frac{d}{A}} \qquad (2)$$

where (I) am current, (V) is the voltage, (d) is the thickness of the sample and (A) is the surface area of the sample. As the electrical conductivity as $1.2x10^{-10}$ S/cm was calculated. The electrical conductivity value calculated for sample has good values for HAP as compared in literature. Also it can be said that insulators are materials having an electrical conductivity σ $<10^{-8}$ S/cm.

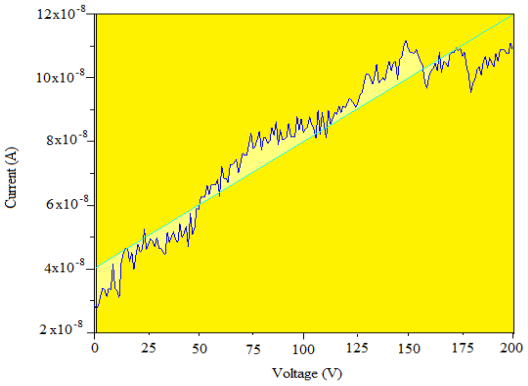

Fig. 11. I-V Characterization curve of the sample

5. CONCLUSION

In this work, hydroxyapatite was prepared via the hydrothermal method. Also characterised of sample determine by XRD, FTIR, I-V, TG-DTA, EDS, SEM, chemical and thermal analyses were used to investigate the structure, morphology, and composition of the obtained product. XRD is used to analyse the structural properties of material, the crystallite size obtained from XRD was found to be 12.2 nm. In I-V characterization of the sample, the electrical conductivity of the sample was obtained as $1.2x10^{-10}$ S/cm and that the electrical conductivity value has importance for HAP considering the literatures. TG-DTA analysis was done to determine the thermal stability, the thermal analysis demonstration the confirm construction of stability compound of the material. Also by used the TGA (thermogravimetric analysis) demonstrates the total weight loss 8.583% in the temperature range from room temperature to 925°C. FTIR is a way used for chemical identification, based on the fact that the selective absorption of material occurs in the infrared region. The most intense peak among the phosphate group was observed in the region of ~720cm^{-1}. SEM has been used to of the obtained HAP. The morphology of HAP sample exhibit shape plate-like structure with a smooth surface.The elemental analysis of the sample was performed by X-ray Energy Dispersive spectroscopy (EDS). The phosphorus, calcium, and oxygen were observed only in obtained EDS spectra of the HAP sample.The best Ca/P ratio for synthesised sample was found to be 1.65.

ACKNOWLEDGEMENTS

This work is financially supported by FÜBAP, Project No: FF.16.14.

REFERENCES

Al-Hazmi, F. E. (2016). "Synthesis and electrical properties of Bi doped hydroxyapatite ceramics." *Journal of Alloys and Compounds*, Vol. 665, pp. 119-123.

Badran, H., I. Yahia, M. S. Hamdy and N. Awwad (2017). "Lithium-doped hydroxyapatite nano-composites: Synthesis, characterization, gamma attenuation coefficient and dielectric properties." *Radiation Physics and Chemistry*, Vol. 130, pp. 85-91.

Brown, P. W. and B. Constantz (1994). *Hydroxyapatite and related materials*. CRC press, USA.

Gümüşderelioğlu, M. (2002). "Biyomalzemeler." *Bilim ve Teknik Dergisi, TÜBİTAK, Temmuz özel sayısı*.

Hench, L. L. and J. Wilson (1993). *An introduction to bioceramics*. USA, World scientific.

Jagadale, P. N., P. P. Jagtap, M. G. Joshi and S. R. Bamane (2016). "A prototype synthesis and characterization of hydroxyapatite bioceramics nanocrystallites." *Advanced Materials Letters*, Vol. 7, No. 4, pp. 325-329.

Orlovskii, V., V. Komlev and S. Barinov (2002). "Hydroxyapatite and hydroxyapatite-based ceramics." *Inorganic Materials*, Vol. 38, No. 10, pp. 973-984.

Padiyan, D. P., A. Marikani and K. Murali (2003). "Influence of thickness and substrate temperature on electrical and photoelectrical properties of vacuum-deposited CdSe thin films." *Materials Chemistry and Physics*, Vol. 78, No. 1, pp. 51-58.

Park, J. B. and J. D. Bronzino (2002). *Biomaterials: principles and applications*, crc press, USA.

Pasinli, A. (2004). "Biyomedikal uygulamalarda kullanılan biyomalzemeler." *Makine Teknolojileri Elektronik Dergisi*, Vol. 4, pp. 25-34.

Sadat-Shojai, M., M.-T. Khorasani, E. Dinpanah-Khoshdargi and A. Jamshidi (2013). "Synthesis methods for nanosized hydroxyapatite with diverse structures." *Acta biomaterialia*, Vol. 9, No. 8, pp. 7591-7621.

Sato, M., M. A. Sambito, A. Aslani, N. M. Kalkhoran, E. B. Slamovich and T. J. Webster (2006). "Increased osteoblast functions on undoped and yttrium-doped nanocrystalline hydroxyapatite coatings on titanium." *Biomaterials*, Vol. 27, No. 11, pp. 2358-2369.

Singh, R. and J. S. Sidhu (2014). "Synthesis and Characterization of Biomaterial Hydroxyapatite." *International Journal of Engineering Sciences & Research Technology* Vol. 3, No. 8, pp. 744-758.

Stanić, V., S. Dimitrijević, J. Antić-Stanković, M. Mitrić, B. Jokić, I. B. Plećaš and S. Raičević (2010). "Synthesis, characterization and antimicrobial activity of copper and zinc-doped hydroxyapatite nanopowders." *Applied Surface Science*, Vol. 256, No. 20, pp. 6083-6089.

Zhang, C., C. Li, S. Huang, Z. Hou, Z. Cheng, P. Yang, C. Peng and J. Lin (2010). "Self-activated luminescent and mesoporous strontium hydroxyapatite nanorods for drug delivery." *Biomaterials*, Vol. 31, No. 12, pp. 3374-3383.

Zhang, X. (2007). *Preparation and characterization of calcium phosphate ceramics and composites as bone substitutes*. University of California, Usa.

Turkish Journal of Engineering

Turkish Journal of Engineering (TUJE)
Vol. 2, Issue 1, pp. 7-11, January 2018
ISSN 2587-1366, Turkey
DOI: 10.31127/tuje.327978
Research Article

AGING EFFECTS ON TRANSFORMATION TEMPERATURES AND ENTHALPIES FOR TiNi ALLOY

Canan Aksu Canbay [1] and İskender Özkul *[2]

[1] Fırat University, Faculty of Science, Department of Physics, Elazığ, Turkey
ORCID ID 0000-0002-5151-4576
caksu@firat.edu.tr

[2] Mersin University, Engineering Faculty, Department of Mechanical Engineering, Mersin, Turkey
ORCID ID 0000-0003-4255-0564
iskender@mersin.edu.tr

* Corresponding Author
Received: 12/07/2017 Accepted: 14/09/2017

ABSTRACT
Shape memory alloys are frequently used today. For this reason, researches are more focused on this subject. In this study, transformation temperature and enthalpy changes caused by aging of TiNi alloy were investigated from thermally induced shape memory alloys. The results obtained from the experiments performed in 21 different aging environments were evaluated by using graphs. The results showed us how effective the variable parameters used in the experiments are on the alloy.

Keywords: *Aging Effect, Shape Memory Alloy, TiNi, DSC, Martensitic Transformation*

1. INTRODUCTION

Nitinol, discovered in the early 1960s, started a new material concept. The superior capabilities of shape memory alloys inspired many applications. This alloy, which has been subject to many applications from the day it was discovered to the present day, has progressed rapidly.

Many areas are used from health to space technology (Birman 1997; Van Humbeeck, 2001; Lagoudas, 2008; Yamauchi *et al.* 2011; Jani *et al.* 2014). The expression showing usage areas according to years is presented in Fig. 1.

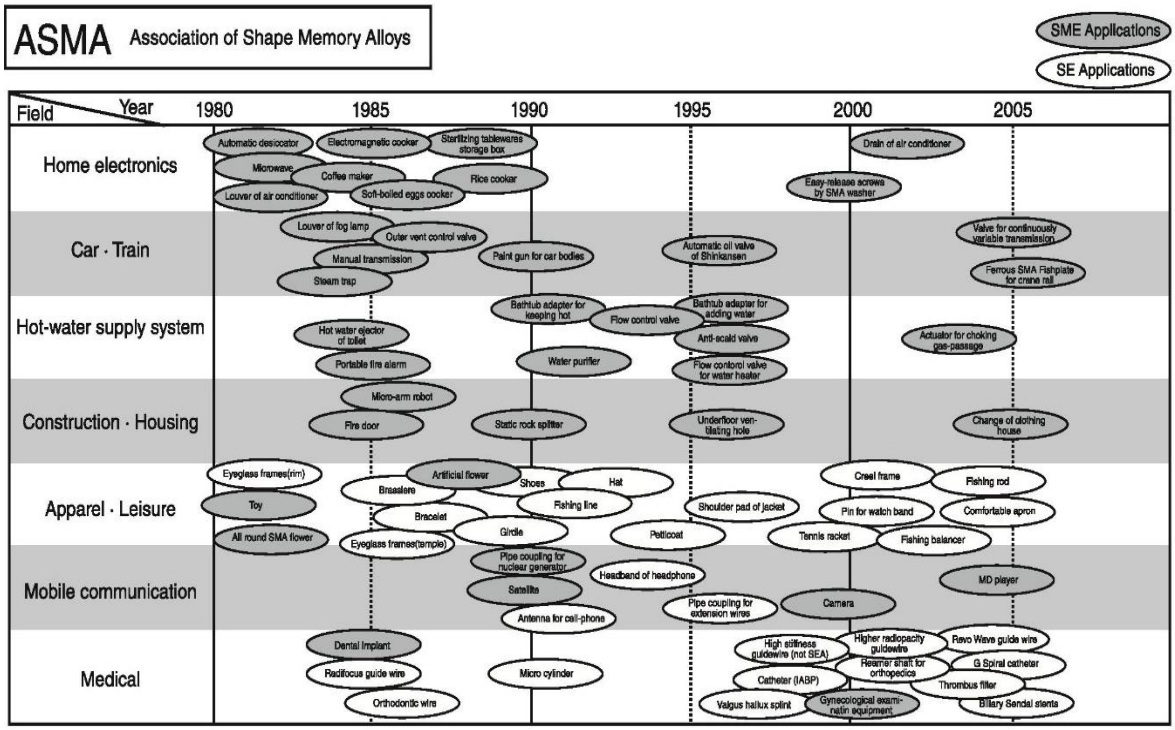

Figure 1. History of SMA application in Japan (Yamauchi, Ohkata, Tsuchiya and Miyazaki 2011)

After the discovery of shape memory alloys, many alloy combinations have been tried. But the most functional of these is the TiNi alloy. It is used very frequently in the health field, especially since it performs very well in biocompatibility. At the same time, it has the attractiveness of having transformation temperatures close to room temperatures (Shabalovskaya, 1996; Es-Souni *et al.* 2005). Shape memory alloys can be induced by many different methods. However, in industrial applications, temperature-inducing alloys are generally used such as thermostat (Wayman, 1993).

Therefore, the alloys used are exposed to heat afterwards. As this cycle continues, an aging occurs on the material. This aging causes changes in the character of the material in the process. This change in material is important in product design, product life and quality (Stachowiak *et al.* 1988; Otubo *et al.* 2008; Frenzel *et al.* 2010; Canbay *et al.* 2017).

In this study, experiments were carried out by aging the commercial TiNi alloy at different aging temperatures and waiting times. The results of the maximum temperature and enthalpy values of the austenite phases of the alloys were obtained with a differential scanning calorimeter (DSC) instrument. The values are then reviewed modeled thanks to 3D graphics.

2. EXPERIMENTAL

In our experimental work we used a commercial product, a 0.7 mm diameter TiNi alloy. We split this alloy into 21 equal parts and made it ready for use in experiments. The chemical composition of the material was obtained by energy dispersive X-ray micro analyzer and the results are shown in Table 1.

Table 1. Specimen chemical composition results

Element	Weight%	Atomic%
Ti	50.62	55.68
Ni	49.38	44.32

In aging experiments, 7 different waiting times were selected at 3 different temperatures. The products obtained by performing 21 tests in total were collected the conversion temperatures and enthalpy values in the DSC device. The results obtained with the parameters of the experiments performed are shown in Table 2.

Table 2. Aged TiNi samples martensite transformation analyze results

Item	A_{max} (C°)	$\Delta H_{M\rightarrow A}$ (J.g^{-1})	M_{max} (C°)	$\Delta H_{A\rightarrow M}$ (J.g^{-1})
200 C° - 0.5h	47.12	-5.43	40.45	3.21
200 C° - 1h	47.08	-3.96	46.94	1.49
200 C° - 3h	46.84	-3.79	40.93	1.74
200 C° - 7h	47.43	-4.40	41.59	2.09
200 C° - 24h	47.08	-3.45	41.01	2.23
200 C° - 36h	47.55	-6.30	41.08	3.11
200 C° - 48h	48.05	-3.81	39.14	1.93
300 C° - 0.5h	47.92	-3.41	43.03	1.32
300 C° - 1h	49.94	-4.49	43.01	2.31
300 C° - 3h	47.59	-5.04	40.73	2.73
300 C° - 7h	53.69	-4.92	47.18	1.9
300 C° - 24h	53.59	-6.24	46.5	3.75
300 C° - 36h	53.97	-4.53	47.51	1.72
300 C° - 48h	54.58	-5.55	47.68	3.71
400 C° - 0.5h	51.25	-4.36	44.46	2.86
400 C° - 1h	51.35	-3.57	44.35	3.2
400 C° - 3h	51.36	-4.09	45.45	2.72
400 C° - 7h	51.8	-4.36	44.59	3.2
400 C° - 24h	51.72	-5.25	44.07	3.98
400 C° - 36h	52.88	-5.58	45.17	4.63
400 C° - 48h	53.97	-5.96	45.81	4.29

Furthermore, the specimens were applied fine polishing and etched with 10%HF-60%HNO_3-30%CH_3COOH solution. Microstructure observations of alloys by optical microscopy are depicted in Fig. 2.

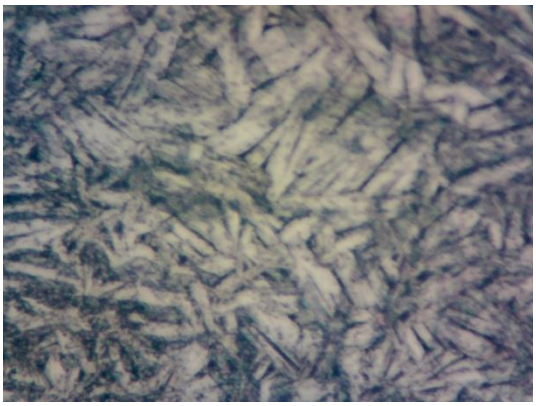

(a) 200 °C – 36 Hours

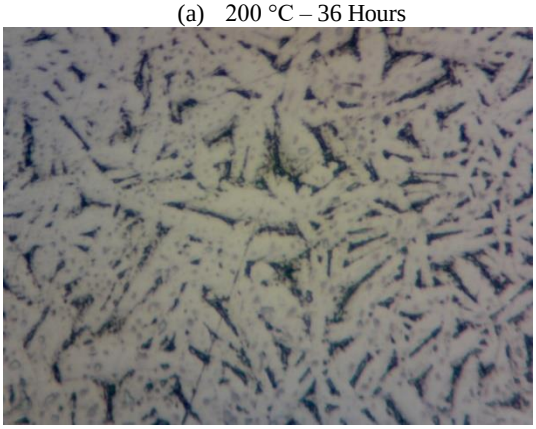

(d) 400 °C – 36 Hours

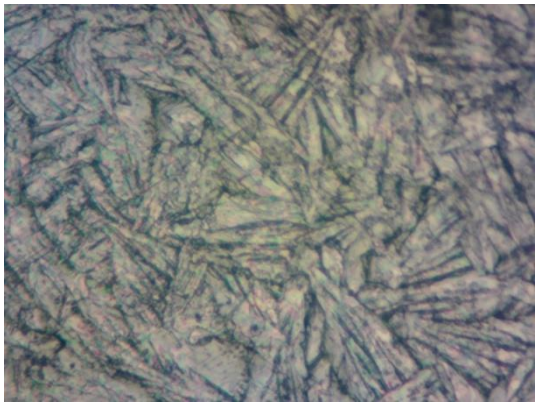

(b) 300 °C – 36 Hours

Fig. 2. The optic micrograph images TiNi Alloys

Fig. 2 shows images of the optical microscope at different temperatures but at the same dwell times. The martensite plates with different orientations in the images are easily observed.

3. DISCUSSION

The results are created as a contour plot using the graphics program. The obtained graphs show the relationship between Amax, Mmax and enthalpy values results with temperature and waiting times. Austenite maximum temperature and martensite maximum temperature values are the tops of the phase change peaks in the DSC graph. The area under the curve is the enthalpy value that represents the amount of energy required during solid state phase transformation and that's shown in Fig. 3.

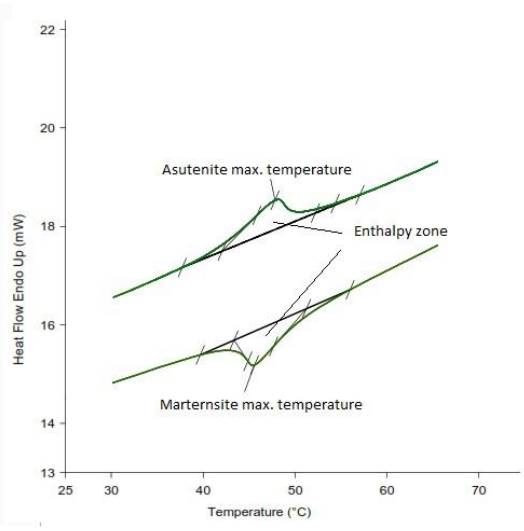

Fig. 3. A sample DSC plot

These values are endothermic and exothermic. This is why the enthalpy values in some of the results obtained are negative. In our study, the 2D contour plots and dynamic models were generated by sigma plot software using the experimental results. The graphs are shown in Fig. 4.

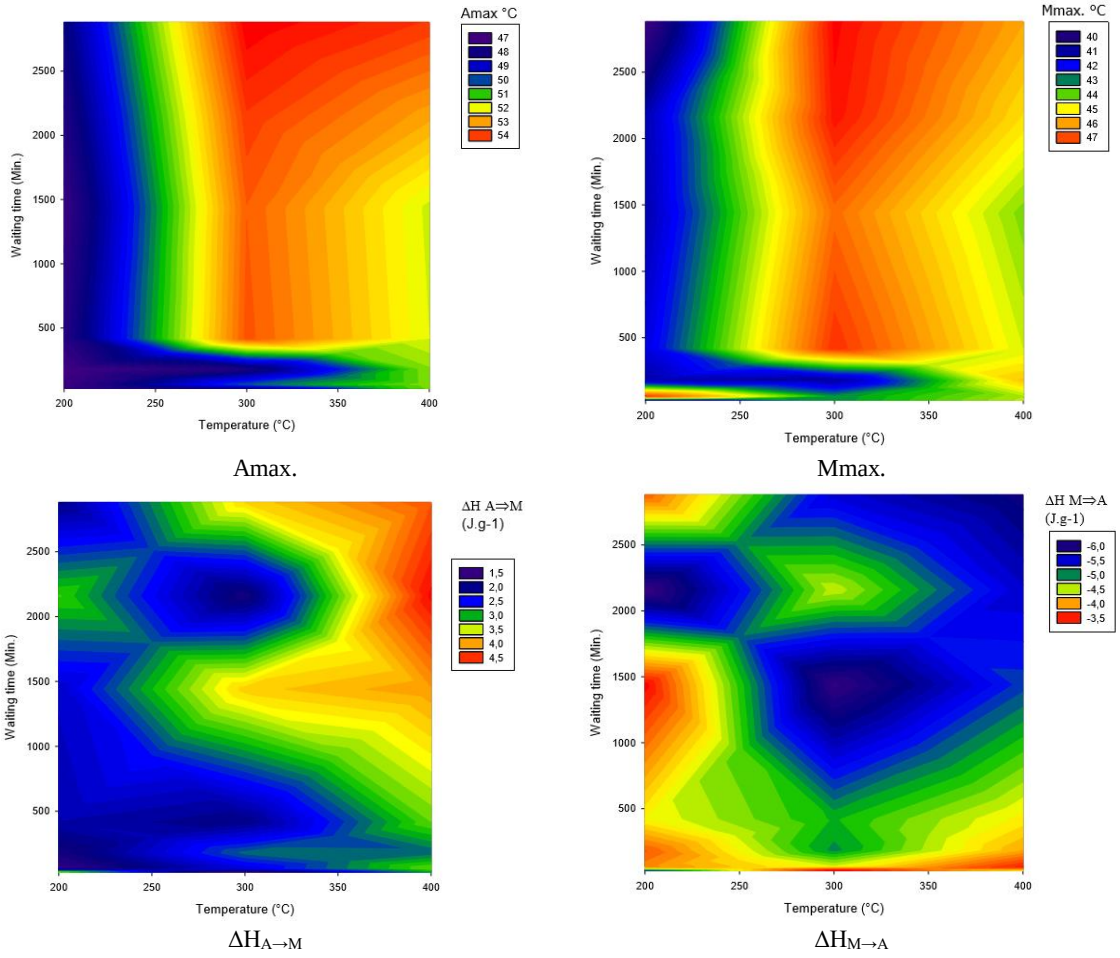

Fig. 4. The contour plots of martensite and austenite phase transformation temperatures and enthalpies

Also, the nonlinear regression - dynamic fitting results are depicted following equations.

$$Amax=25.8559+0.1398*(AT)+0.0017*(WT)-0.0002*(AT)^2+-2{,}4(10^{-7})(WT)^2 \quad (1)$$

$$Mmax=-23.3457-0.1287*(AT)-0.0009*(WT)-0.0006*(AT)^2+5.79(10^{-7})(WT)^2 \quad (2)$$

$$\Delta H_{A\rightarrow M}=-4.2743-0.0551*(AT)-0.0008*(WT)-4.15(10^{-5})*(AT)^2-4.77(10^{-7})(WT)^2 \quad (3)$$

$$\Delta H_{M\rightarrow A}=-5.5329-0.0564*(AT)-0.0030*(WT)-2.89(10^{-5})*(AT)^2+2{,}43(10^{-7})(WT)^2 \quad (4)$$

In Fig. 4, the Amax. And Mmax. a smooth transition was observed along the temperature axis. These transitions in the opposite direction is decreased after 300 degrees. The greatest change in temperature deviations was seen at 300 degrees relative to these graphs. However, an irregularity in the transit at the horizontal line corresponding to 60 minutes is clearly visible. The defection in this section is caused by residual stresses of the alloy. It was seen that the stresses on the material did not cause any trouble during the high waiting periods. When the enthalpy graphs are examined, it is determined that there are different soft passages but there are regional distortions and irregularities at 300 degrees. The colour ranges on the enthalpy charts are different because they are endothermic and exothermic reactions.

4. RESULTS

It is very important to know the character of the material when designing the product. The changes in the aging process of TiNi alloys, which are in the class of smart materials and have the most use, have been investigated. In our study, Ti55.68Ni44.32 (at.%) alloys were tested at 7 waiting times at 3 different temperature values. The austenite and martensite max temperature values determined by the results obtained by the DSC device and graphs of enthalpy changes were generated. As a result of the graphics, an increase of up to 300 degrees was found to be followed by a decrease in martensite and austenite maximum temperatures. These transitions cannot be observed due to waste stresses around 60 degrees. Enthalpy values have not been found in a regular transition but regional variations have occurred at 300 degrees.

REFERENCES

Birman, V. (1997). "Review of mechanics of shape memory alloy structures." *Applied Mechanics Reviews*, Vol. 50, No., pp. 629-646.

Canbay, C. A., A. Tekataş and İ. Özkul (2017). "Fabrication of Cu-Al-Ni Shape Memory Thin Film By

Thermal Evopration." *Turkish Journal of Engineering (TUJE)*, Vol. 1, No. 2, pp. 27-32.

Es-Souni, M., M. Es-Souni and H. Fischer-Brandies (2005). "Assessing the biocompatibility of NiTi shape memory alloys used for medical applications." *Analytical and bioanalytical chemistry*, Vol. 381, No. 3, pp. 557-567.

Frenzel, J., E. P. George, A. Dlouhy, C. Somsen, M.-X. Wagner and G. Eggeler (2010). "Influence of Ni on martensitic phase transformations in NiTi shape memory alloys." *Acta Materialia*, Vol. 58, No. 9, pp. 3444-3458.

Jani, J. M., M. Leary, A. Subic and M. A. Gibson (2014). "A review of shape memory alloy research, applications and opportunities." *Materials & Design*, Vol. 56, No., pp. 1078-1113.

Lagoudas, D. C. (2008). *Shape memory alloys: modeling and engineering applications*, Springer Science & Business Media, Usa.

Otubo, J., O. Rigo, A. Coelho, C. M. Neto and P. Mei (2008). "The influence of carbon and oxygen content on the martensitic transformation temperatures and enthalpies of NiTi shape memory alloy." *Materials Science and Engineering: A*, Vol. 481, No., pp. 639-642.

Shabalovskaya, S. A. (1996). "On the nature of the biocompatibility and on medical applications of NiTi shape memory and superelastic alloys." *Bio-medical materials and engineering*, Vol. 6, No. 4, pp. 267-289.

Stachowiak, G. and P. McCormick (1988). "Shape memory behaviour associated with the R and martensitic transformations in a NiTi alloy." *Acta Metallurgica*, Vol. 36, No. 2, pp. 291-297.

Van Humbeeck, J. (2001). "Shape memory alloys: a material and a technology." *Advanced Engineering Materials*, Vol. 3, No. 11, pp. 837-850.

Wayman, C. (1993). "Shape memory alloys." *MRS bulletin*, Vol. 18, No. 4, pp. 49-56.

Yamauchi, K., I. Ohkata, K. Tsuchiya and S. Miyazaki (2011). *Shape memory and superelastic alloys: Applications and technologies*, Elsevier.

Turkish Journal of Engineering

Turkish Journal of Engineering (TUJE)
Vol. 2, Issue 1, pp. 12-16, January 2018
ISSN 2587-1366, Turkey
DOI: 10.31127/tuje.334004
Research Article

THE EFFECT OF SODIUM CARBONATE ON ELEVATED TEMPERATURE RESISTANCE OF CEMENT MORTARS CONTAINING NATURAL ZEOLITE

Cahit Bilim *[1]

[1] Mersin University, Engineering Faculty, Department of Civil Engineering, Mersin, Turkey
ORCID ID 0000-0002-0975-1391
cbilim@mersin.edu.tr

* Corresponding Author

Received: 10/08/2017 Accepted: 15/09/2017

ABSTRACT
In this paper, the effect of sodium carbonate (Na_2CO_3) on the flexural and compressive strength of cement mortars containing natural zeolite subjected to high temperatures were examined. The results obtained from the tests were compared with the reference mortars. In the mortar mixtures, sand and water quantities were kept constant. Water/binder and sand/binder ratios were 0.5 and 3.0, respectively. In the mixtures, the crushed sand was used and ordinary Portland cement (OPC) was replaced with 5, 10, 15 and 20% natural zeolite by weight. For activation of zeolite, sodium carbonate having 7% Na dosage was used as an activator. The findings showed that the resistance of mortars subjected to high temperatures were dependent on the temperature level, and that the fire resistance of zeolite mortars was higher than that of mortar made with OPC only. Additionally, it was seen from the test results that Na_2CO_3 used for activation in zeolite mortars led to a decrease in the flexural and compressive strength values after the high temperatures.

Keywords: *Fire Resistance, Mortar, Zeolite, Activator*

1. INTRODUCTION

Portland cement is an important building material that is incorporated into concrete and is widely used today in the world. However, remarkable energy requirements and significant emissions of carbon dioxide to atmospheres as well as the use of natural resources lead to serious environmental problems in the production of cement. High energy costs and environmental problems resulting from the production process make it necessary to develop sustainable binder systems that can be an alternative to cement in the construction industry. One of the alternative methods of reducing cement consumption is the use of pozzolans in concrete production. The use of pozzolans in the construction sector, where building elements in large volumes are produced, will not only save energy but will also contribute to the solution of environmental problems. One of the pozzolans that can be used in concrete is natural zeolites that have emerged as an important binder material in recent years. Zeolite tuffs contain alumina silicate just as pozzolans which are used as additives in cement (Lea, 1970; Poon *et al.*, 1999). Studies performing on pozzolanic activity have shown that zeolitic tuffs have excellent pozzolanic activity (Drzaj *et al.*, 1978), and they are more reactive than glassy materials in terms of lime fixation (Massazza, 1998; Sersale, 1995). Their some physical and chemical properties such as low specific gravity, pore structure and silica content enable zeolites to be used in many industrial areas like pollution management, energy, agriculture, stock farming and mine metallurgy (Kurudirek *et al.*, 2010; Bilim, 2014). They also possess special properties such as ion exchange, molecular sieves, a large surface area and catalytic activity (Breck, 1971). The investigations on concretes containing natural zeolite have shown that zeolite improves concrete properties and can be used in high performance concrete production due to its high pozzolanic activity (Feng *et al.*, 1990; Perraki *et al.*, 2003; Canpolat *et al.*, 2004). Natural zeolites have good pozzolanic activity and their use as partial replacement of OPC lead to an increase in durability of cement and concrete composites (Najimi *et al.*, 2012). The use of natural zeolite in concrete causes less strength loss in early ages and contributes to the development of strength by reducing the porosity of the binder material (Poon *et al.*, 1999). Due to the pores in the structure of natural zeolites, superplasticizing chemical admixture is needed in the mixture (Fragoulis *et al.*, 1997; Quanlin and Naiqian, 2005). Natural zeolite also prevents the undesirable expansions resulting from sulfate attack and alkali aggregate reaction (Janotka and Števula, 1998; Uzal *et al.*, 2003). Other hand, the studies carried out in recent years have showed that natural pozzolan as well as industrial wastes could be used as raw materials in geopolymer binders (Allahverdi *et al.*, 2008). In other study, Yousef *et al.* (2009) produced geopolymer concrete samples using Jordan zeolitic tuffs and compared them with kaolin incorporated geopolymers. According to the experimental data, the compressive strength of geopolymers containing zeolitic tuff was higher than that of kaolin added geopolymers. Furthermore, the samples containing zeolitic tuffs had lower densities and higher water absorption rates. As a result, they concluded that zeolitic tuffs could be utilized in geopolymer production. Additionally, Davidovits (2008) have noted that geopolymerization of alumina silicate-containing materials such as fly ash, coal slag, blast furnace slag, silica fume, volcanic tuff, depends on the applied temperature and duration.

As seen, various research results on this material have been reported. The findings have showed that it is possible to evaluate natural zeolites, which are present in great quantities in our country, as a cementitious material instead of industrial by-products such as silica fume, fly ash and blast furnace slag in case of some factors such as not being close to the industrial waste zone, expenditures in transporting the waste, harmful compounds in the waste. In addition to the limited data obtained from the tests, the lack of research on the use of natural zeolites as a cement / concrete mineral admixture is negatively affecting the widespread use of natural zeolites in the construction sector. In order to overcome this problem, more research findings need to be published in the literature and still, many properties related to zeolite wait to be explored. For example, fire resistance of mortars and concretes with zeolite has received almost no attention. Therefore, within the scope of this paper, the compressive and flexural strengths of zeolite incorporated mortars with and without Na_2CO_3 subjected to high temperatures were investigated.

2. EXPERIMENTAL PROGRAM

In the study, OPC conforming to the requirements of TS EN 197-1 (2012) class 42.5R was used as reference binder. Table 1 presents chemical compositions and physical properties for OPC and ground natural zeolite supplied by Manisa/Gördes region. On the other hand, Fig. 1 shows the mineralogical results investigated by using X-ray diffraction (XRD; Rigaku, Tokyo, Japan, Miniflex II with a nickel filtered Cu Kα) for natural zeolite which consists of clinoptilolite as the primary phase, and which contains small amounts of quartz.

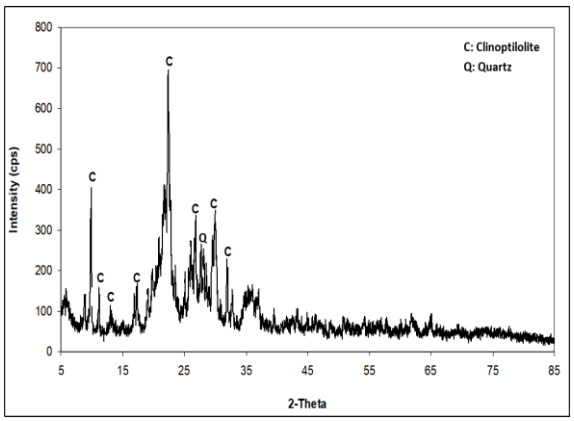

Fig. 1. XRD analysis of Gördes natural zeolite

In the mixtures, superplasticizer, drinkable tap water and crushed sand with a maximum size of 4 mm were used. While determining superplasticizer dosages, the flow values of zeolite incorporated mortars were maintained in the vicinity of ± 10% of the flow value obtained from OPC mortar. Cement was replaced with 5, 10, 15 and 20% zeolite by weight. A w/b ratio of 0.5 was used to prepare mortar samples. The sand to cementitious binder ratio was 3:1. In the mortars containing Na_2CO_3, the Na dosage was 7% according to mass of zeolite.

Table 1. Chemical compositions and physical properties of cement and zeolite

Oxides (%)	Cement	Zeolite	Physical properties of Portland cement	
SiO_2	20.65	63.01	Specific gravity	3.15
CaO	63.15	3.87	Initial setting time (min)	186
Al_2O_3	4.75	10.72	Final setting time (min)	230
Fe_2O_3	3.05	2.68	Volume expansion (mm)	1.0
MgO	3.55	1.07	Blaine specific surface (cm^2/g)	3250
SO_3	2.52	0.22	Compressive strength (MPa) of cement	
Na_2O	0.13	0.23	2 days	27.8
K_2O	0.74	3.80	7 days	42.1
LOI	1.10	14.00	28 days	52.3
IR	0.94	-	Physical properties of zeolite	
Free CaO	0.91	-	Specific gravity	2.17
			Specific surface (Blaine) (cm^2/g)	9660
			Pozzolanic activity index (%) of clinoptilolite	
			7 days	58
			28 days	81

A summary of the experimental program is presented in Table 2.

Table 2. The experimental program

Mix.	Cement	Zeolite	Superplasticizer	Na
Z0	100%	-	-	-
Z5	-	5%	1.25%	-
Z10	-	10%	2.30%	-
Z15	-	15%	3.50%	-
Z20	-	20%	4.50%	-
Z5N	-	5%	1.50%	7%
Z10N	-	10%	2.70%	7%
Z15N	-	15%	4.00%	7%
Z20N	-	20%	5.00%	7%

To produce the mortars, firstly, superplasticizer added water, Na_2CO_3 and zeolite were placed in the mortar mixer and blended in slow mode for 30 s and then, the crushed sand was poured for 30 s while continuing to mix in slow mode. Next, the mixture was blended in fast mode for 30 s and then stopped and held for 15 s, followed by further mixing for 60 s in fast mode (TS EN 196-1, 2009). Eventually, the fresh mortar mixtures were taken from the mixer and cast into sample moulds with 40 x 40 x 160 mm dimensions. Then, to obtain a good compaction, the samples were jolted 60 times in 1 min. Samples were demoulded 24 h after casting and were kept in water at a temperature of 20 °C for 27 days. After the curing period, the samples were removed from water and the test procedure was performed. For the elevated temperature resistance tests, three samples of each mortar mixture were exposed to 300, 600 and 900 °C temperatures for 1 h in furnace. The heating rate was set at 5 °C/min up to reach the target temperature. Then, the hot mortar samples were kept in furnace. After the cooling period to laboratory temperature, the compressive and flexural strength values of samples were determined according to TS EN 1015-11 (2000). The compressive strength test was carried out using six broken pieces of test prisms remained from the flexural strength tests performed on three samples. The test results were compared with those of unheated control mortar at 20 °C.

3. RESULTS AND DISCUSSION

3.1. Residual Compressive Strength after High Temperatures

The residual compressive strength results of mortars after exposure to 300, 600 and 900°C temperatures are presented in Table 3.

Table 3. Compressive strengths of mortars (MPa)

		Cooled in furnace		
	20°C	300°C	600°C	900°C
Z0	53.48	55.11	16.69	2.06
Z5	54.22	58.25	26.00	9.29
Z10	54.74	59.10	32.21	9.69
Z15	42.52	48.83	31.81	5.26
Z20	39.91	47.85	24.96	4.15
Z5N	33.00	34.52	24.14	3.94
Z10N	36.15	32.44	25.89	4.07
Z15N	27.30	29.78	20.08	1.78
Z20N	26.59	28.86	18.10	1.53

According to Table 3, at 20 °C, the OPC mortar (Z0) achieved a compressive strength of 53.48 MPa while the compressive strengths of the mortars containing zeolite ranged from 39.91 MPa to 54.74 MPa. The increment up to 10% in zeolite content of mixtures increased the compressive strength values for mortar specimens at this temperature (20 °C). For example, the increment in the compressive strength of mortar containing 10% zeolite (Z10) was approximately 3%, compared to the mixture containing 100% OPC (Z0). In zeolite mortars containing Na_2CO_3, the compressive strengths values ranged from 26.59 MPa to 36.15 MPa. The increase in zeolite amount of mixture for a constant Na dosage of 7% decreased the compressive strengths for mortar specimens at 20 °C.

At 300 °C, the compressive strengths of zeolite incorporated mortars ranged from 47.85 MPa to 59.10 MPa while the compressive strength of OPC mortar (Z0) was 55.11 MPa. The increase up to 10% in zeolite amount increased the compressive strength values for mortar

specimens at this temperature (300 °C). For example, the increment in the compressive strength of mortar containing 10% zeolite (Z10) was approximately 7% in comparison with 100% OPC mortar (Z0). The compressive strengths values ranged from 28.86 MPa to 34.52 MPa for Na_2CO_3 added mortars containing zeolite. Namely, the use of Na_2CO_3 in zeolite mortars reduced the compressive strength values at 300 °C. Additionally, an increase was observed in the compressive strengths of all mortar samples exposed to 300 °C temperature in comparison with the mortar samples at 20 °C. This increase observed in strength may depend on the relief of pressures in the course of drying, which also leads to greater van der Waals forces resulting from a closer formation of capillary pores (Aydın *et al.*, 2008).

After 600 °C, although the compressive strength of all mortars began to decrease seriously, the performance of mortars containing zeolite was better than OPC mortar. For example, at 900 °C, the compressive strength of OPC mortar (Z0) was 2.06 MPa while the compressive strengths of zeolite added mortars were between 4.15 MPa and 9.69 MPa. At this temperature, the mortar with the highest strength was the Z10 mixture having 10% zeolite content. Other hand, the mortars containing Na_2CO_3 had the lowest compressive strengths among zeolite added mortars. The compressive strengths of these mortars varied between 1.53 MPa and 4.07 MPa. These significant losses occurring in the compressive strength values of mortars after 900°C temperature may be attributed to the disintegration of calcium silicate hydrate gel (Poon *et al.*, 2001; Xu *et al.*, 2001).

3.2. Residual Flexural Strength after High Temperatures

The residual flexural strength results of mortars after exposure to 300, 600 and 900°C temperatures are presented in Table 4.

Table 4. Flexural strengths of mortars (MPa)

		Cooled in furnace		
	20ºC	300ºC	600ºC	900ºC
Z0	10.31	7.70	2.39	1.27
Z5	10.97	9.72	3.60	2.13
Z10	10.69	9.07	4.66	1.75
Z15	9.68	8.51	4.71	1.36
Z20	8.84	8.10	3.37	1.00
Z5N	7.36	6.05	4.06	2.03
Z10N	7.50	6.45	4.08	2.41
Z15N	7.17	3.42	2.16	1.01
Z20N	7.52	2.69	1.05	0

As seen in Table 4, at 20 °C, the flexural strength of OPC mortar (Z0) was 10.31 MPa while the flexural strengths of the mortars containing zeolite varied from 8.84 MPa to 10.97 MPa. The zeolite substitution made after 10% in the mixtures began to decrease the flexural strength values for mortar specimens at this temperature (20 °C). Moreover, it was seen that the addition of Na_2CO_3 having a Na dosage of 7% into mixtures containing zeolite negatively affected the flexural strength. As a result of this, zeolite incorporated mortars containing Na_2CO_3 exhibited the flexural strengths ranging from 7.17 MPa to 7.52 MPa.

The harmful effects of high temperatures on the flexural strength were more evident than the case in the compressive strength. In this regard, although all mortars increased their compressive strength up to 300°C, they lost the flexural strengths as from 300 °C. On other hand, at 600 °C, the flexural strengths for all of mortars were between 1.05 MPa and 4.71 MPa while they showed the flexural strength values varying from 1.01 MPa to 2.41 MPa at 900 °C temperature. Also, the flexural strength of the mortar (Z20N) containing 7% Na and 20% zeolite could not be determined at 900 °C. The explanation for these low flexural strengths obtained from the tests is as follows: thermal cracks occur from the important temperature differences between the core and the surface of sample cross section (Kong and Sanjayan, 2010). The presence of these cracks decreases the valid area of cross sections and the existence of tensile stresses below the neutral axis in the samples exposed to the flexural test brings about the increase in size of cracks (Özturan and Cülfik, 2002; Xu *et al.*, 2003; Li *et al.*, 2004). Therefore, the effect of cracks on the flexural strength value is more evident than on the compressive strength value due to the drop in the valid area of cross section which resists the stresses (Bilim, 2014). Also, the mixtures containing Na_2CO_3 had the lowest flexural strengths among zeolite mortars for both 600 °C and 900 °C temperatures.

4. CONCLUSION

The following conclusions can be drawn from this study:

1. The replacement of zeolite up to 10% with OPC improved the mechanical strengths of mortars kept at room temperatures. Additionally, all mortars containing zeolite showed generally better performance to high temperatures such as 900 °C than OPC mortar.
2. The resistances of mortars subjected to elevated temperatures were determined to be dependent on the temperature level.
3. The detrimental effect of high temperatures on the flexural strength was more severe than the case in the compressive strength.
4. It was seen that the use of Na_2CO_3 as an activator in mortars containing zeolite reduced both the compressive strengths and the flexural strengths for all temperatures studied within the scope of this research. For this reason, it is considered that the researches on the mixtures containing zeolite activated by different alkaline activators such as water glass or sodium hydroxide should be carried out.

REFERENCES

Allahverdi, A., Mehrpour, K. and Kani, E. N. (2008). "Taftan pozzolan-based geopolymer cement." *IUST International Journal of Engineering Science*, Vol. 19, No. 3, pp. 1-5.

Aydın, S., Yazıcı, H. and Baradan, B. (2008). "High temperature resistance of normal strength and autoclaved high strength mortar incorporated polypropylene and steel fibers." *Construction and Building Materials*, Vol. 22, No. 4, pp. 504-512.

Bilim, C. (2014). "The influence of clinoptilolite replacement on the durability of cement mortars." *Journal of Materials in Civil Engineering*, Vol. 26, No. 3, pp. 520-526.

Breck, D. W. (1971). *Zeolite molecular sieves: structure*, New York: Wiley Chemistry and Uses.

Canpolat, F., Yılmaz, K., Köse, M. M., Sümer, M. and Yurdusev, M. A. (2004). "Use of zeolite, coal bottom ash and fly ash as replacement materials in cement production." *Cement and Concrete Research*, Vol. 34, No. 5, pp. 731-735.

Davıdovits, J. (2008). *Geopolymer Chemistry and applications*, Saint Quantin, France.

Drzaj, B., Hocevar, S. and Slokan, M. (1978). "Kinetic and mechanism of reaction in the zeolitic tuff–CaO–H_2O systems at increased temperatures." *Cement and Concrete Research*, Vol. 8, No. 6, pp. 711-720.

Feng, N. Q., Li, G. Z. and Zang, X. W. (1990). "High-strength and flowing concrete with a zeolitic mineral admixture." *Cement and Concrete Aggregates*, Vol. 12, No. 2, pp. 61-69.

Fragoulis, D., Chaniotakis, E. and Stamatakis, M. G. (1997). "Zeolitic tuffs of Kimolos Island, Aegean Sea, Greece and their industrial potential." *Cement and Concrete Research*, Vol. 27, No. 6, pp. 889-905.

Janotka, I. and Števula, L. (1998). "Effect of bentonite and zeolite on durability of cement suspension under sulfate attack." *ACI Materials Journal*, Vol. 96, No. 6, pp. 710-715.

Kong, D. L. Y. and Sanjayan, J. G. (2010). "Effect of elevated temperatures on geopolymer paste, mortar and concrete." *Cement and Concrete Research*, Vol. 40, No. 2, pp. 334-339.

Lea, F. M. (1970). *The Chemistry of cement and concrete*, 3rd ed. London: Edward Arnold Ltd.; 1970. ISBN: 0 7131 22773.

Li, M., Qian, C. and Sun, W. (2004). "Mechanical properties of high strength concrete after fire." *Cement and Concrete Research*, Vol. 34, No. 6, pp. 1001-1005.

Massazza, F. (1998). *Pozzolana and pozzolanic cements*, in: P.C. Hewlett (Ed.), Lea's Chemistry of Cement and Concrete, 4th Edition, Elsevier Ltd., London.

Najimi, M., Sobhani, J., Ahmadi, B. and Shekarchi, M. (2012). "An experimental study on durability properties of concrete containing zeolite as a highly reactive natural pozzolan." *Construction and Building Materials*, Vol. 35, No. 10, pp. 1023-1033.

Özturan, T. and Cülfik, M. S. (2002). "Effect of elevated temperatures on the residual mechanical properties of high-performance mortar." *Cement and Concrete Research*, Vol. 32, No. 5, pp. 809-816.

Perraki, T., Kakali, G. and Kontoleon, F. (2003). "The effect of natural zeolites on the early hydration of portland cement." *Microporous and Mesoporous Materials*, Vol. 61, No. 1–3, pp. 205-212.

Poon, C. S., Lam, L., Kou, S. C. and Lin, Z. S. (1999). "A study on the hydration rate of natural zeolite blended cement pastes." *Construction and Building Materials*, Vol. 13, No. 8, pp. 427-432.

Poon, C. S., Azhar, S., Anson, M. and Wong, Y. L. (2001). "Comparison of the strength and durability performance of normal- and high-strength pozzolanic concretes at elevated temperatures." *Cement and Concrete Research*, Vol. 31, No. 9, pp. 1291-1300.

Quanlin, N. and Naiqian, F. (2005). "Effect of modified zeolite on the expansion of alkaline silica reaction." *Cement and Concrete Research*, Vol. 35, No. 9, pp.1784-1788.

Sersale, R. (1995). "Zeolite tuff as a pozzolanic addition in the manufacture of blended cements." *in: D.W. Ming, F.A. Mumpton (Eds.), Natural Zeolites '93: Occurrence, Properties and Use International Committee of Natural Zeolites*, New York, pp. 603-612.

TS EN 196-1 (2009). *Methods of testing cement-Part 1: Determination of strength*, Turkish Standard Institute, Ankara, Turkey.

TSI, TS EN 197-1 (2012). *Cement-Part 1: Compositions and conformity criteria for common cements*, Turkish Standard Institute, Ankara, Turkey.

TSI, TS EN 1015-11 (2000). *Methods of test for mortar for masonry-Part 11: Determination of flexural and compressive strength of hardened mortar*, Turkish Standard Institute, Ankara, Turkey.

Uzal, B., Bektaş, F. and Turanlı, L. (2003). "Öğütülmüş doğal zeolitin alkali-silika reaksiyonu ve sülfat reaksiyonu etkisi ile genleşmesinin incelenmesi." *5. Ulusal Beton Kongresi (Betonun Dayanıklılığı)*, İstanbul, Turkey.

Xu, Y., Wong, Y. L., Poon, C. S. and Anson, M. (2001). "Impact of high temperature on PFA concrete." *Cement and Concrete Research*, Vol. 31, No. 7, pp. 1065-1073.

Xu, Y., Wong, Y. L., Poon, C. S. and Anson, M. (2003). "Influence of PFA on cracking of concrete and cement paste after exposure to high temperatures." *Cement and Concrete Research*, Vol. 33, No. 12, pp. 2009-2016.

Yousef, R. I., El-Eswed, B., Alshaaer, M., Khalili, F. and Khoury, H. (2009). "The influence of using Jordanian natural zeolite on the adsorption, physical, and mechanical properties of geopolymers products." *Journal of Hazardous Materials*, Vol. 165, No. 1-3, pp. 379-387.

Turkish Journal of Engineering

Turkish Journal of Engineering (TUJE)
Vol. 2, Issue 1, pp. 17-21, January 2018
ISSN 2587-1366, Turkey
DOI: 10.31127/tuje.330658
Research Article

LIGHTWEIGHT FOAM IMPACT ATTENUATOR DESIGN FOR FORMULA SAE CAR

Emre İsa Albak *[1], Erol Solmaz [2], Necmettin Kaya [3] and Ferruh Öztürk [4]

[1] Uludağ University, Engineering Faculty, Automotive Engineering Department, Bursa, Turkey
ORCID ID 0000-0001-9215-0775
emrealbak@uludag.edu.tr

[2] Uludağ University, Engineering Faculty, Automotive Engineering Department, Bursa, Turkey
ORCID ID 0000-0001-9369-3552
esolmaz@uludag.edu.tr

[3] Uludağ University, Engineering Faculty, Mechanical Engineering Department, Bursa, Turkey
ORCID ID 0000-0002-8297-0777
necmi@uludag.edu.tr

[4] Uludağ University, Engineering Faculty, Automotive Engineering Department, Bursa, Turkey
ORCID ID 0000-0001-5767-8312
ferruh@uludag.edu.tr

* Corresponding Author
Received: 24/07/2017 Accepted: 22/09/2017

ABSTRACT
The impact attenuator is a safety component which is used to reduce the effects of frontal crash on driver, which can cause injuries. This article describes the design process of the impact attenuator with lightweight materials to satisfy the required weight reduction targets for Formula SAE racing car. This study is carried out as part of weight reduction studies on Formula SAE racing car. As a first step, the impact-absorbing structures and technical features were compared. In this step, it was decided to use EPP foam material with a density of 100 g/l as basic material to design a lightweight impact attenuator. Also, the design outlines of shape and analysis techniques for impact attenuator was defined in this step. Then, validation process was carried out for virtual model of 100 g/l EPP foam material. Foam material model was validated using reference study in literature. After model validation, a new impact attenuator was designed according to Formula SAE rules. It is 10% lighter than the standard model. The results show that selected EPP foam material can be used to design a lightweight impact attenuator for formula SAE race car to satisfy weight reduction requirements successfully.

Keywords: *Impact Attenuator, EPP, Foam, Formula SAE, Formula Student*

1. INTRODUCTION

The Formula SAE competitions are one of the most important engineering competitions held in over 13 countries around the world and participated by over 500 college teams. In these competitions, racing car designs are evaluated in different categories for all the design stages. There are many categories such as cost analysis, engineering design and performance. The weight reduction studies for Formula SAE car are taken considerable attention recent years due to green design concepts in car design. This article describes the design process of the impact attenuator with lightweight materials to satisfy the required weight reduction targets for Formula SAE racing car. The impact attenuator is a safety component which is used to reduce the effects of frontal crash on driver, which can cause injuries.

Although there are several research papers in literature regarding weight reduction and frontal crash structures of car body, there are only a few works regarding design of Formula SAE racing car impact attenuator. Benchmarking study was also carried out to examine the design outline and specifications of other Formula SAE racing cars and their safety components. One of the most important safety criteria during the design of a racing car is the characteristic behavior of the vehicle in the event of a crash (Boria, 2014). Safety in the event of an accident is important not only in Formula 1 vehicles but also in Formula SAE vehicles (Belingardi *et al*., 2010). In high-speed accidents, special structures are designed to absorb kinetic energy that will affect the human body (Obradovich *et al*., 2012). The energy damping structures which are used in Formula SAE racing cars are impact attenuators. Impact attenuators should be lightweight for better performance such as better acceleration, better steering, and easier maintenance for the vehicle's handling dynamics (Enomoto *et al*., 2007). For this reason, impact attenuator materials must be made from lightweight materials to ensure high performance criteria (Munusamy *et al*., 2010). Materials such as aluminum, honeycomb, carbon, foam are usually used for impact attenuators.

Foams are used in different areas in many sectors due to their low density and high energy damping properties. They are widely used in passive safety systems in modern vehicles in the automotive sector (Slik *et al*., 2006). Many types of foam materials are used in the automotive industry. One of them is expanded polypropylene (EPP). The energy absorption capacity and lightness properties of the EPP material are key features that enable it to be used as an energy absorbing pad in the automotive industry (Yıldızhan *et al*., 2016). EPP foams are used as sandwich material in crush boxes in automotive industry due to low weight and high energy damping, and as impact protectors in side door panels (Bouix *et al*., 2009).

The Uludağ Racing team has used a standard impact attenuator made from Impaxx 700 foam (Impaxx) and the weight is 700 gr. This study describes the design process of the new lightweight impact attenuator which was designed according to Formula SAE rules. EPP foam material with a density of 100 g/l as basic material was selected to design a lightweight impact attenuator. Also, the design outlines of shape and analysis techniques were defined in the first design step. Then, validation process was carried out for finite element model of 100 g/l EPP foam material. The results of the physical drop test at the initial speed of 2.2 m/s to the 50 mm cubic sample were taken as reference points to validate the material model. After model validation, a lightweight impact attenuator was designed according to Formula SAE rules. The results show that selected EPP foam material can be used successfully to design a lightweight impact attenuator for formula SAE race car to satisfy weight reduction requirements.

The following sections describe the design of a foam impact attenuator to satisfy weight reduction requirements for the Formula SAE racing car.

2. ULUDAĞ RACING TEAM AND IMPACT ATTENUATOR

Uludağ Racing Team (URT) was established in 2011 to produce cars for Formula SAE competitions under the Uludağ University Automotive Community. URT have produced four racing cars. The last one was produced in year of 2017. First participation of URT to Formula SAE Racing Car Competition was in 2011 in UK. Second and third participations took place in the following years competitions which were organized in Italy and Russia. URT won two rewards from these competitions.

2.1. Impact Attenuator

The impact attenuator is one of the most important parts in terms of safety in Formula SAE vehicles. The specific requirements of impact attenuator are outlined in FSAE rules which are given as follows:

- At least 200 mm (7.8 in) long, with its length oriented along the fore/aft axis of the Frame;
- At least 100 mm (3.9 in) high and 200 mm (7.8 in) wide for a minimum distance of 200 mm (7.8 in) forward of the Front Bulkhead (2017-18 Formula SAE® Rules, 2016).

The desired dynamic test conditions for interrogating the impact attenuator stiffness are given below:

Test data that proves that the Impact Attenuator Assembly, when mounted on the front of a vehicle with a total mass of 300 kg (661 lbs.) and impacting a solid, non-yielding impact barrier with a velocity of impact of 7.0 meters/second (23.0 ft./sec), decelerates the vehicle at a rate not exceeding 20 g's average and 40 g's peak. The energy absorbed in this event must meet or exceed 7350 Joules (2017-18 Formula SAE® Rules, 2016).

3. IMPACT ATTENUATOR DESIGN AND SIMULATIONS

Finite element simulations are important to check how well the required properties are achieved in the design process. Two different simulation studies were conducted in this study. The first study is the validation of the material model of EPP. The second study is dynamic finite element simulation according to Formula SAE rules. Hyperworks Student 2017 Edition software was used for finite element modeling and analysis. The finite element model of the structure was developed by means of the software code Hypermesh. Finally, the crash event simulation has been developed by means of the Radioss code.

3.1. Validation of EPP 100 g/l Material Model

EPP material with 100 g/l density was selected for impact attenuator. In order to validate the material model, finite element simulations were carried out. The stress-strain curves to define the material model for the EPP are given in Fig. 1. These curves were taken from a 50-mm cubic specimen of 90 kg of mass at the initial speed of 2.2 m/s followed by a drop test conducted by Untaroiu *et al.* (2010).

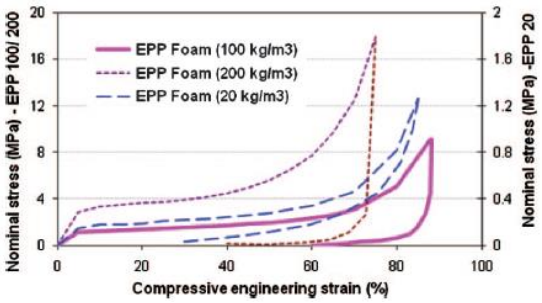

Fig. 1. EPP 100 g/l foam material Strain-Stress Curves (Untaroiu *et al.*, 2010)

To define the EPP foam material model, LAW70 material card and P14_solid property card were used. Stress-strain curve was defining in Radioss solver code (Altair University). Material card and the property card information are given in Table 1. The values used for the property are the values recommended for the foam element in the Radioss Manuals.

Cubic specimen of 50 mm dimensions was modeled with first order hexahedral elements. Rigid wall was defined as 90 kg mass and the drop velocity is 2.2 m/s. In order to achieve the same test conditions, six degrees of freedom of the underside of the specimen was also constrained (see Fig. 2).

Table 1. Material card and property card specifications for foam material

Material Cards	(MAT70)
Rho_Initial	1.0e-10 (Mg/mm^3)
E0 (Initial Young's Modulus)	230.0 MPa
Failure Plastic Strain	0.9
Property Card	(P14_SOLID)
ISOLID	24
Ismstr	11
I_strain	1

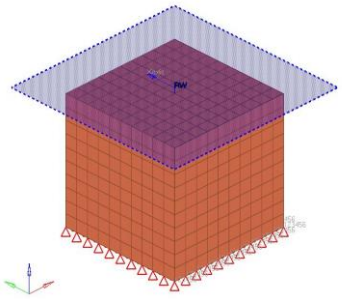

Fig. 2. Validation model of EPP foam material

The comparison of finite element drop analysis and Untaroiu *et al.* (2010)'s test results is given in Fig. 3. It is seen that the strain-stress results are in very good correlation (Fig. 3). According to this result, the selected material card for the foam material and the property card can be used in the analysis of the dynamic finite element analysis.

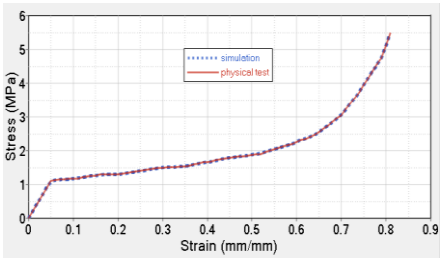

Fig. 3. Correlation results of simulation and physical test

3.2. Impact Attenuator Dynamic Simulation

A dynamic finite element analysis was conducted for the suitability of the designed impact attenuator to the Formula SAE rules. The requirements for the dynamic model according to the rules are that the vehicle with a mass of 300 kg is hit with a rigid wall at the initial velocity of 7m/s. It is required that the energy of the 7350 J energy is absorbed and the deceleration is 20 g average and 40 g maximum.

The dynamic model consists of the chassis, anti-intrusion plate, impact attenuator, mass, the rigid wall and rigid elements. The finite element model is shown in Fig. 4.

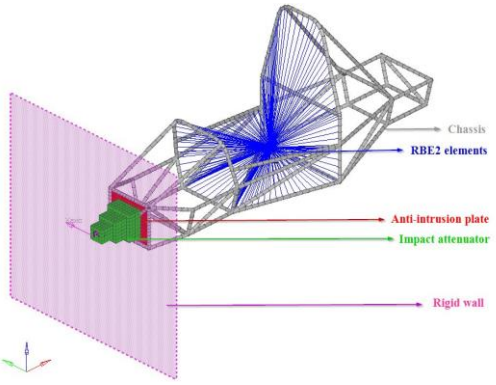

Fig. 4. Simulation model of Formula SAE Car

The chassis was modeled with beam elements with 50 mm element size. Anti-intrusion plate thickness is 2mm. It allows the foam material to be fixed to the chassis, was modeled with 25 mm first order 2D quad elements. The impact attenuator was modeled with first order hexahedral elements with 25 mm element dimensions (Fig. 5 on the right). The connections were made with rigid elements of RBE2.

Fig. 5 represents the model of current impact attenuator and new impact attenuator. Current impact attenuator weight is 700 gr and new impact attenuator is 632 gr. Impact attenuator's mass was decreased about 10%.

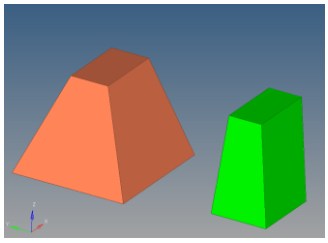

Fig. 5. Impact attenuators (current model on the left, new model on the right)

The finite element analysis results are shown in Fig. 6 and Fig. 7. In Fig. 6, the dots represent the initial position of the chassis and it is seen that the impact attenuator reduces the speed of the vehicle to zero. Fig. 7 shows the shape of the impact attenuator depending on the time.

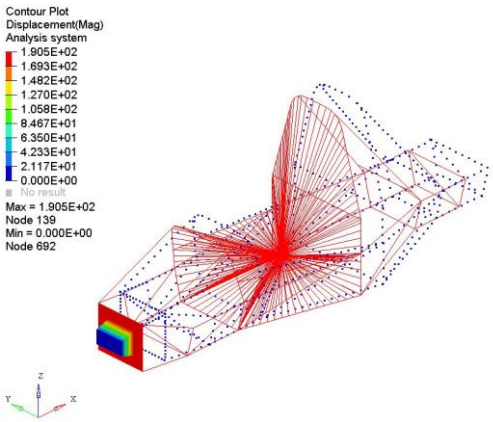

Fig. 6. Finite element crash simulation results

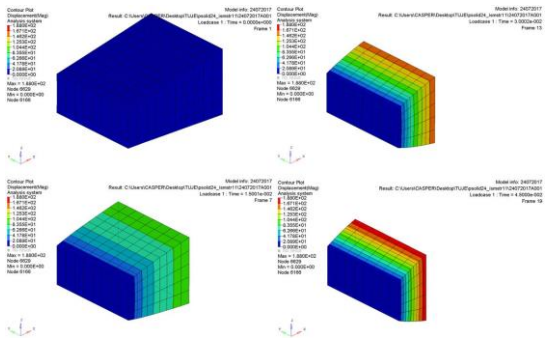

Fig. 7. Displacement results after crash

Fig. 8 shows the deceleration of the vehicle versus time. Deceleration increases as the foam compresses, and about the velocity is 0 m/s, it takes its maximum values and falls rapidly afterwards. Deceleration value of the vehicle reaches a maximum of 30 g and the average deceleration value is less than 20 g. All deceleration results are in accordance with the rules.

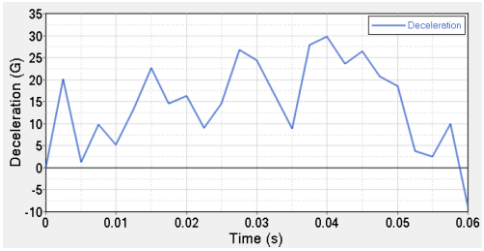

Fig. 8. Deceleration results of crash simulation of Formula SAE Car

As shown in Fig. 9, the amount of energy absorbed increases as expected and there is a backward movement when the vehicle speed is zero. The maximum amount of absorbed energy is 7420 J, which is above the minimum required by the Formula SAE rules. Therefore, it has been shown that using a foam as a crash absorbing material which is lighter but provides the desired conditions can be used for such Formula SAE vehicles.

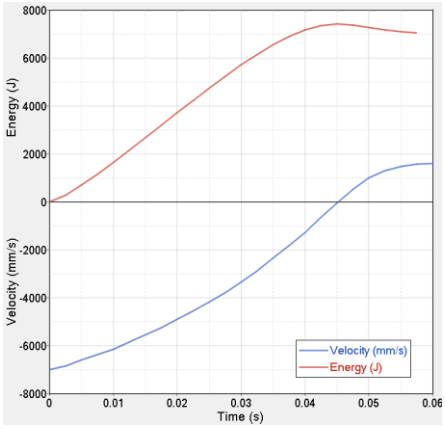

Fig. 9. Energy and velocity results of dynamic simulation

4. CONCLUSION

In this study, 10% lighter impact attenuator compared to the standard model was designed to satisfy weight reduction requirements for the Formula SAE racing car. It was found that the foam impact attenuator can be used successfully to satisfy the required Formula SAE racing car specifications regarding the deceleration and energy absorbing criteria. This study was carried out as part of weight reduction studies on Formula SAE racing car.

In future work, further weight reduction and new structural design will be enhanced by creating an optimization model for the foam impact attenuator. In addition, designs with different materials and structural topology will be tried for new impact attenuator which can also be used for other vehicles, not just for Formula SAE racing cars.

REFERENCES

2017-18 Formula SAE® Rules. 2016. SAE International.

Altair University, (http://www.altairuniversity.com/wp-content/uploads/2011/10/RADIOSS_10.0_Reference_Guide2.pdf) [Access 14 July 2017].

Belingardi, G., Obradovic, J. (2010). ‘‘Design of the Impact Attenuator for a Formula Student Racing Car: Numerical Simulation of the Impact Crash Test.’’ *Journal of the Serbian Society for Computational Mechanics*, Vol. 4, No. 1, pp. 52-65.

Boria, S. (2010). ‘‘Behaviour of an Impact Attenuator for Formula SAE Car under Dynamic Loading.’’ *International Journal of Vehicle Structures and Systems*, Vol.2, No. 2, pp. 45-53.

Bouix, R., Viot, P., Lataillade, J., (2009). ‘‘Polypropylene foam behaviour under dynamic loadings: Strain rate, density and microstructure effects.’’ *International Journal of Impact Engineering*, Vol. 36, No. 2, pp. 329-342

Enomoto, H., Miyazaki, Y., Mizuno, H., Hirano, E., Kitayama, S., Yamazaki, K., Uota, N. (2007) ‘‘Development of CFRP Monocoque Front ImpactAttenuator for FSAE with VaRTM.’’ *Society of Automotive Engineers of Japan*, 2007-32-0120.

Impaxx, (https://www.fsaeonline.com/page.aspx?pageid=193613e4-fff1-4ea9-97ec-eb1c07fbe3c0) [Access 14 July 2017].

Munusamy, R., Barton, D. (2010).‘‘Lightweight impact crash attenuators for a small Formula SAE race car.’’ *International Journal of Crashworthiness*, Vol. 15, No.2, pp. 223-234.

Obradovic, J., Boria, S., Belingardi, G. (2012). ‘‘Lightweight design and crash analysis of composite frontal impact energy absorbing structures.’’ *Composite Structures*, Vol. 94, No. 2, pp. 423-430.

Slik, G., Vogel, G., Chawda, V., (2006). **‘‘**Material Model Validation of a High Efficient Energy Absorbing Foam.**’’** 5th LS-DYNA Forum, Ulm.

Untaroiu,C., Shin, J., Crandall, J., Fredriksson. R., Bostrom, O., Takahashi, Y., Akiyama, A., Okmoto, M., Kikuchi, Y. (2010). ‘‘Development and validation of pedestrian sedan bucks using finite-element simulations: a numerical investigation of the influence of vehicle automatic braking on the kinematics of the pedestrian involved in vehicle collisions.’’ *International Journal of Crashworthiness*, Vol. 15, No. 5, pp. 491–503

Yıldızhan, M., Efendioğlu B., Kaya, N., Öztürk, İ., Albak E., Öztürk, F. (2016). ‘‘Design of improved energy absorbing pads to reduce occupant injuries in vehicle side impact.’’ *International Journal of Vehicle Design*, Vol. 71, No. 1/2/3/4, pp. 174-190.

Turkish Journal of Engineering

Turkish Journal of Engineering (TUJE)
Vol. 2, Issue 1, pp. 22-26, January 2018
ISSN 2587-1366, Turkey
DOI: 10.31127/tuje.330672
Research Article

GALVANIC CORROSION OF ZINC ANODE AND COPPER CATHODE CELL

Nurettin Çek *[1]

[1] Fırat University, Faculty of Engineering, Department of Metallurgical and Materials Engineering, Elazığ, Turkey
ORCID ID 0000-0001-6120-9228
nurettincek001@gmail.com

* Corresponding Author
Received: 24/07/2017 Accepted: 22/09/2017

ABSTRACT
Detection and control of galvanic corrosion is a critical aspect of engineering for the chemical processes used in the fabrication of metals, alloys and materials industry. Galvanic corrosion can occur when two metals having different status in the electrochemical ambient are configured in mutual interaction within the galvanic cell structure and are exposed to the ion conducting electrolyte. In this study, ion-containing water was used as an electrolyte, the zinc as the anode electrode, copper as the cathode was used as an electrode, and a galvanic cell was fabricated. The formation of corrosion products with time on zinc anode reduced the voltage and current in galvanic cell considerable and anode film layer of considerable increase. Time-dependent experiments have provided good sources of information about the performance of the zinc anode electrode and the copper cathode electrode in the galvanic cell.

Keywords: *Zinc, Copper, Electrode, Galvanic Cell, Corrosion*

1. INTRODUCTION

Corrosion is the chemical and physical properties of metal and metal-like materials event change. The extensive use of metal in the process of daily life and the resulting metal corrosion has caused challenging problems. Corrosion of metals are a terrible waste both of economic and natural resources. Metals are suffering corrosion because they want to return to their natural oxide form (Ammal *et al.*, 2017). There are many factors that affect corrosion. For example; with biofilm formation, corrosion is occurring (Cordas *et al.*, 2008).

Various methods have been applied to prevent inhibit corrosion. These methods typically include: Use of alloys in place of pure metal, improvement of metal plating (organic or inorganic), improvement of metal design (avoiding excessive stress, minimizing indentation), electrochemical protection (anodic protection, reduced temperature, reduced speed liquid, removing oxygen from the environment, reduced the concentration of the solution, use of corrosion inhibitors) etc. applications (Çek, 2014, Cicek, 2017). Corrosion applications are galvanic cell of one example. The type of corrosion that occurs in the galvanic cell is called as galvanic corrosion. The galvanic cell basically consists of the anode electrode, cathode electrode and an electrolyte (water, moisture, ionic liquid etc.). Galvanic corrosion is perceptible in heat exchangers, pipelines, cooling towers, and in each status in which two different metals materials come in contact in the presence of water or moisture (Shi *et al.*, 2012; Hasan, 2014, Cicek, 2017). Example; in the study conducted by Çek (2014), corrosion of copper in the aqueous medium was prevented by using vaseline. Therefore, galvanic corrosion in copper is inhibited. Vaseline is an organic material obtained from petroleum and is often used to heal wound (Çek, 2014; Bhupinder and Manju, 2015).

In the galvanic cell, voltage and current generated values by anode and cathode electrodes are an important parameter affecting corrosion. The use of materials with minimum potential (voltage) differences would minimize corrosion in a galvanic cell. In addition, low current (ampere) production in the galvanic cell reduces usually corrosion (Taher and Al Jabab, 2003). Galvanic corrosion is one of the major problems to the use of zinc materials in the industry. During the galvanic corrosion process of zinc's, the zinc ions react and precipitate in the form of oxides or hydroxides (Song *et al.*, 2004). Therefore, detailed information about the time-dependent galvanic corrosion of the zinc materials should be obtained. In this study for this purpose, the zinc as anode electrode the copper as the cathode electrode and ionic conductive water as the electrolyte was used. The corrosion effect of the anode and cathode electrodes was studied based on time dependent voltage and current measurements on the galvanic cell.

2. MATERIALS AND METHOD

2.1. Materials

Materials and apparatus properties were as follows. Zinc (Zn) plate electrodes; 99.9% purity, 3.060 grams, each electrode has 4 cm length and 4.5 cm wide. Copper cylinder rod electrodes; 99.9% purity, 3 grams, 8 cm length, 0.75 cm diameter. Digital multimeter (UNI-T: UT61C) was used to make for direct current and voltage measurements. Resistance, 980 ohm (Ω). Digital pH meter (616.0.001, ISOLAB). Sensitive Scale (PKS 360-3, KERN). Plastic box shaped like a truncated cone (4 cm bottom diameter, 7 cm ceiling diameter, 8 cm diameter) and the empty volume of the plastic box chamber was 191.68 cm^3 (191.68 milliliter (mL)). Water is pH value about at 7.65 and it content includes sodium (Na), potassium (K), magnesium (Mg), calcium (Ca) cations and fluorine (F), chlorine (Cl), sulphate (SO_4) anion.

2.2. Method

Weight (gram (g)) measurements are made with the precision weighing instrument (Sensitive Scale). Weight measurements were made before and after use of the electrodes of the galvanic cell. The total surface area (191.68 cm^3) of the plastic box has about at 191.68 mL water intake capacity. After, zinc as anode electrode and copper as cathode electrode was used in the plastic box. Therefore, galvanic cell was designed.

The galvanic cell was subjected to daily electrical measurements according to resistance-dependent and non-resistance-related conditions. In addition, oxide layer in manufactured galvanic cell, the time-dependent states of the anode and cathode electrodes, corrosion etc. factors have been detected. Discussions were held in regard to the formation, development and effects of these factors on the system. In this study, galvanic cell model is shown in Fig. 1.

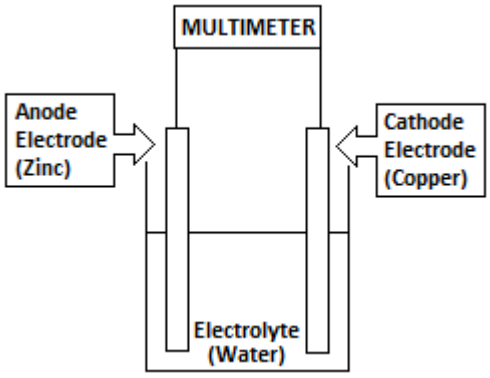

Fig. 1. Galvanic cell model of in this study

3. RESULTS AND DISCUSSION

As the zinc plate (-) load electrode and as the copper cylinder rod (+) load electrode the worked. This situation was detected by the multimeter. Without external load (resistance) on galvanic cells are open-circuit voltage (V_{OC}) and short-circuit current (I_{SC}) values measured by the multimeter. Volt (V_R) and current (I_R) values were measured by multimeter while the galvanic cells were connected to the external load (resistance). Resistance is not constantly connected to the galvanic cell; it is only connected during measurements. Time-dependent electrical generation values of galvanic cells are in shown in Table 1.

Table 1. Electrical measurements of first type galvanic cell

Time (Day)	V_{OC} (mV)	I_{SC} (µA)	V_R (mV)	I_R (µA)
1	360	33	2	3
2	180	14	1	1
3	181	1	0.5	0.5
4	152	0.5	0.2	0.3
5	67	0.3	0.2	0.2
6	60	0.2	0.1	0.1

According to Table 1, the zinc anode initially experienced a very rapid galvanic corrosion process. The rate of galvanic corrosion decreased with time in the zinc anode. Therefore, electrical (V_{OC}, I_{SC}, V_R and I_R) values decreased. The change in electrical values is evidence of galvanic corrosion. According to Table 1, the current values increase as the voltage values increased. In addition, the corrosion of the anode zinc electrode occurs whether or not it is resistance. But, the corrosion state is different when there is resistance and when there is no resistance. After 6 days, the colorless water was red colored and a red precipitate was observed under the plastic box (Fig. 4.). Due to galvanic corrosion of zinc anode, white rust first film layer formed and then red rust film layer formed. The zinc anode electrode image in the first 6 days is shown in Fig. 2.

Fig. 2. The zinc anode state in the first 6 days

Upon this, the water in the plastic box was drained, the plastic container was cleaned with clean water, and the plastic container was re-filled with clean water. Electrical measurements were made again and the results similar to the results (±10 mV of V_{OC}, ±10 µA of I_{SC}, ±0.05 mV of V_R, ±0.05 µA of I_R) in Table 1 were obtained. Observations made the additional 6 days more the first 6 days showed that the area covered by the oxide film layer increased and that red precipitate accumulated at the plastic box.

At the end of all these 12 days, the zinc anode electrode was removed from the galvanic cell, it was washed with clean water and dried in the environment (1 hour) and weigh measurement was made. At the end of 12 days, zinc anode electrode weight (W_{finish}) was measured as 3.030 gr.

Fig. 3. The zinc anode status in the second 6 days (total 12 days)

The electrodes on the galvanic cell and the appearance of red colored water (electrolyte) are shown in Fig 4.

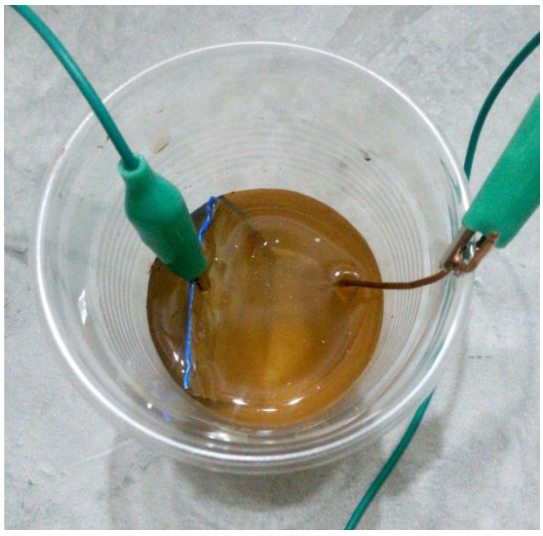

Fig. 4. The electrodes and electrolyte on the galvanic cell

The oxide layer dominates more area in Fig. 3 than Fig. 2.

Weight loss is the proof of corrosion and corrosion rate (CR) is measuring to the formula in Equation (1) (Ammal *et al.*, 2017; Tribak *et al.*,2017)

$$CR=\frac{\mathbf{W}}{\mathbf{A.t}} \quad (1)$$

Where, W is the difference between starting weight (W_{start}) and end weight (W_{finish}), A is the surface area of immersed anode metal and t is time (hours) of application. In this study; W_{start} is 3.060 grams, W_{finish} is 3.030 grams, W_{change} is 0.030 g (30 mg), A is 18 cm^2, t is 288 hours (12 days). The corrosion rate (CR) in this study is calculated in Equation (2).

$$CR=\frac{30}{18.288}=0.005 \text{ mg/cm}^2\text{h} \quad (2)$$

Another issue to be taken into account in corrosion rate calculations is current density. Current density is shown in Equation (3).

$$\text{Current density}=\frac{\text{Ampere (A)}}{\text{Anode surface area (cm}^2\text{)}} \quad (3)$$

In this study, current density is shown in Table 2.

Table 2. In this study current density

Time (Day)	Current density (not resistance)	Current density (Resistance connect)
1	$18.33\text{x}10^{-7}$	$1.66\text{x}10^{-7}$
2	$7.77\text{x}10^{-7}$	$0.55\text{x}10^{-7}$
3	$0.55\text{x}10^{-7}$	$0.27\text{x}10^{-7}$
4	$0.27\text{x}10^{-7}$	$0.16\text{x}10^{-7}$
5	$0.16\text{x}10^{-7}$	$0.11\text{x}10^{-7}$
6	$0.11\text{x}10^{-7}$	$0.05\text{x}10^{-7}$

According to literature as the current density increases, the corrosion rate (CR) increases (Bardal, 2007). The corrosion rate due to current density is calculated as in Equation (4).

$$CR=\frac{I.M}{z.F.p} \text{ cm/s} \quad \text{(Bardal, 2007)} \quad (4)$$

Where, I is current density ($\mu A/cm^2$), M is mol mass of the anode (65.38 g/mol atom of Zn), z is number of electrons in the reaction equation for the anodic reaction (dissolution reaction) (per atom of the dissolving metal) ($2e^-$ of Zn), F is Faraday constant (96485 C/mol e^-), p is density of anode (7.14 g/cm^3 of Zn), Using the equation (4), the data in Table 3 was obtained.

Table 3. Corrosion rate (CR) due to current density

Time (Day)	CR (cm/s) (not resistance)	CR (cm/s) (resistance connect)
1	$8.69\text{x}10^{-11}$	$7.88\text{x}10^{-11}$
2	$3.68\text{x}10^{-11}$	$2.63\text{x}10^{-11}$
3	$2.63\text{x}10^{-11}$	$1.28\text{x}10^{-11}$
4	$1.28\text{x}10^{-11}$	$0.75\text{x}10^{-11}$
5	$0.75\text{x}10^{-11}$	$0.52\text{x}10^{-11}$
6	$0.52\text{x}10^{-11}$	$0.27\text{x}10^{-11}$

A constant corrosion rate is desirable for the calculations to be the healthy and long term. However, as shown in Table 3, the corrosion rate in this work is not constant.

The annual corrosion rate is calculated using Equation (5).

$$CR=3268\frac{I.M}{z.p} \text{ mm/year} \quad \text{(Bardal, 2007)} \quad (5)$$

Since the corrosion current and the current density are not constant, an annual corrosion rate (CR) scenario is established for each current and current density obtained. The annual corrosion rates of the different electrical values according to different days are given in Table 4.

Table 4. In this study corrosion rate (CR) scenario of year

Time (Day)	CR (mm/year) (not resistance)	CR (mm/year) (Resistance connect)
1	0.02742	0.00248
2	0.01162	0.00082
3	0.00082	0.00040
4	0.00040	0.00023
5	0.00023	0.00016
6	0.00016	0.00007

According to the table 4, the corrosion rate is reducing daily. If the galvanic cell was regularly maintained at the initial current intensities, the annual corrosion rate (CR) obtained would be 0.02742 mm/year without resistance and 0.00248 mm/year with resistance. The lowest corrosion rate was achieved on the 6^{th} day. If the galvanic cell was regularly maintained at the 6^{th} day current intensities, the annual corrosion rate (CR) obtained would be 0.00248 mm/year without resistance and 0.00007 mm/year with resistance.

5. CONCLUSION

The zinc anode electrode is not a material that can withstand long-term corrosion. The cathode electrode is protected until the anode electrode is depleted. During this time the copper cathode electrode is not affected corrosion by values measurable.

The formation of the oxide film (rust) on the surface of the zinc anode electrode has been increased with the decrease of voltage and current values at the galvanic cell. After 6 days the electrolyte (water) of the galvanic cell was renewed. The materials precipitate under the plastic box and the rust in the face of the anode were cleaned away with clean water. However, current and voltage values approaching to their first state. But, the current and voltage values are reducing again due to rust formation on the zinc anode electrode surface. This shows that the oxide film (rust) layer reduces the corrosion rate.

One of the important findings obtained in this study is that the current increases as the voltage increases and the current decreases as the voltage decreases. The corrosion rate increases as the current and current density increase (Bardal, 2007). In addition to this, in this study, it has been determined that the voltage values and the corrosion rate (CR) are directly proportional.

Adding on the galvanic cell of electrical resistance has also reduced and slowed down the corrosion as it reduces voltage and current. This is a positive finding. Use of electrical resistance to reduce the negative effects of corrosion on places such as galvanic cells will be a useful application.

ACKNOWLEDGEMENTS

Koç Holding and Arçelik thanks for the experimental instruments. I thank Prof. Dr. Mustafa Aksoy for his scientific supports.

REFERENCES

Ammal, P. R., Prajila, M., Joseph, A. (2017). "Physicochemical studies on the inhibitive properties of a 1,2,4-triazole Schiff's base, HMATD, on the corrosion of mild steel in hydrochloric acid." *Egyptian Journal of Petroleum.* (In press)

Bardal, A. (2007). *Corrosion and Protection Engineering Materials and Processes,* Springer Science&Business Media, USA.

Bhupinder, M. and Manju, M. (2015). *Organic Chemistry*, PHI Learning Pvt. Ltd., Delhi, India.

Cordas, C. M., Guerra, L. T., Xavier, C., Moura, J. J. G. (2008). "Electroactive biofilms of sulphate reducing bacteria." *Electrochimica Acta*, Vol. 54, pp. 29-34.

Çek, N. (2014). "Reduction of copper corrosion effect using vaseline", *13th International Corrosion Symposium*, Elazığ, Turkey, pp. 155-158.

Hasan, B. O. (2014). "Galvanic corrosion of carbon steel–brass couple in chloride containing water and the effect of different parameters." *Journal of Petroleum Science and Engineering*, Vol. 124, pp. 137-145.

Shi, X., Rock, S. E., Turk, M. C., Roy, D. (2012). "Minimizing the effects of galvanic corrosion during chemical mechanical planarization of aluminum in moderately acidic slurry solutions." *Materials Chemistry and Physics*, Vol. 136, pp. 1027-1037.

Song, G., Johannesson, B., Hapugoda, S., StJohn, D. (2004). "Galvanic corrosion of magnesium alloy AZ91D in contact with an aluminium alloy, steel and zinc." *Corrosion Science*, Vol. 46, pp. 955-977.

Cicek, V. (2017). *Corrosion Engineering and Cathodic Protection Handbook: With an Extensive Question and Answer Section*. John Wiley&Sons, USA.

Taher, N. M. and Al Jabab, A. S. (2003). "Galvanic corrosion behavior of implant suprastructure dental alloys." *Dental Materials*, Vol. 19, No. 1, pp. 54-59.

Tribak, Z., Haoudi, A., Skalli, M. K., Rodi, Y. K., El Azzouzi, M., Aouniti, A., Hammouti, B., Senhaji, O. (2017). "5-Chloro-1H-indole-2,3-dione derivative as corrosion inhibitor for mild steel in 1M H_3PO_4: weight loss, electrochemical and SEM studies." *Journal of Materials and Environmental Sciences*, Vol. 8, No. 1, pp. 298-309.

Turkish Journal of Engineering

Turkish Journal of Engineering (TUJE)
Vol. 2, Issue 1, pp. 27-34, January 2018
ISSN 2587-1366, Turkey
DOI: 10.31127/tuje.341462
Research Article

APPLICABILITY OF SOLAR AND WIND ENERGY TECHNOLOGIES FOR A NON-RESIDENTIAL BUILDING

Burhan Bayhan [1] and Gökhan Arslan *[2]

[1] Mersin University, Engineering Faculty, Department of Mechanical Engineering, Mersin, Turkey
ORCID ID 0000-0003-4708-1138
burhanbayhan@mersin.edu.tr

[2] Mersin University, Engineering Faculty, Department of Mechanical Engineering, Mersin, Turkey
ORCID ID 0000-0002-2611-1740
garslan@mersin.edu.tr

* Corresponding Author
Received: 03/10/2017 Accepted: 09/11/2017

ABSTRACT
In this study, applicability of wind and solar energy technologies in a non-residential building located in Mersin, Turkey is investigated. As the non-residential building, a polyclinic was examined. Meteorological data was obtained from Turkish State Meteorological Service to investigate the solar and wind energy technologies. The data was examined statistically. By using wind turbine with 0.9 kW rated power, 2223.5 kWh electricity energy was generated. Similarly, PV panel with 20 % panel efficiency, 5kW total power and 15 m^2 surface area, 4240 kWh electricity energy was generated. Annual energy consumption of the polyclinic was calculated 26107.52 kWh by using EnergyPlus software. To meet heating and cooling loads of the polyclinic, the air source heat pump was preferred. 8.51 % of the total demand can be supplied from wind turbine and 16.24 % by photovoltaic panels. The proposed wind-solar hybrid system for investigated region is not applicable due to low of the wind energy potential of the investigated region, the high price of the wind turbine and the proximity to the lifetime of the utilized components in the system to depreciation time. On the other hand, by using only photovoltaic panels system to generate electricity, it was determined that depreciation time will decrease from 17 to 11 years.

Keywords: *Wind Energy, Solar Energy, Photovoltaic Panel, Heating Load, Cooling Load*

1. INTRODUCTION

The use of renewable energy sources has become important due to the limited life of fossil fuels and their hazard to nature. That topic is now very attractive issue in order to reduce energy dependency on the energy side in terms of Turkey. It is known that one third of the energy expenditure in our country is spent for non-residential buildings, especially for office buildings, and buildings equipped with air conditioning systems hold an important place within this group **(**WECTNC, 2002). For this reason, increasing the use of renewable energy technologies in non-residential buildings is important.

The aim of this study is to investigate the applicability of wind and solar energy technologies in a non-residential building in Mersin, Turkey. Mersin is located on the south region of Turkey and has a coast to the Mediterranean Sea. As a non-residential building, a polyclinic belonging to the public was examined. The main common applications of wind and solar energy technologies are about electricity generation. Therefore, wind turbine and photovoltaic panels are emphasized.

The climate data file for EnergyPlus software, which is used to calculate the heating and cooling loads of a non-residential building, is available in Turkey only for Istanbul, Izmir and Ankara. The climate data file for Mersin was created according to the data obtained from Turkish State Meteorological Service. This study is generally considered as a regional feasibility assessment.

2. LITERATURE REVIEW

In the literature, numerous studies are available about the application of wind and solar energy technologies in buildings. Brief literature rewiev is as follow.

Panapakidis *et al.* (2012) examined PV-Diesel, PV-Wind, Wind-Diesel and Wind-Fuel cell hybrid systems for different sites of Greece. Bekele *et al.* (2012) investigated the possibility of supplying electricity from a solar–wind hybrid system to a remotely located model community in Ethiopian remote region. Islam *et al.* (2012) and Hoque *et al*. (2012) modelled PV–wind–diesel generator hybrid power system for St. Martin Island and a village in Comilla respectively. Lal and Raturi (2012) investigated the feasibility of a wind–PV–diesel generator based hybrid power system for a remote location on the island of Vanua Levu, Fiji. Essalaimeh *et al*. (2013) showed an experimental investigation of using a combination of solar and wind energies as hybrid system for electrical generation under the Jordanian climate conditions. Nogueira *et al*. (2014) have developed model for sizing a PV–wind–battery hybrid energy system, which is applicable for a small rural property in the south of Brazil. Rohani and Nour (2014) modelled and design PV array- wind turbines-batteries-diesel generators hybrid system for the remote area in the western region of Abu Dhabi. Dalwadi and Mehta (2012) examines the feasibility of PV–wind hybrid system for six different locations of Indian state Gujrat. Meherchandani *et al*. (2012) discuss the economic feasibility of standalone hybrid power system consisting of biomass–PV–wind for electrical requirements of a remote rural area in Rajasthan. Vani and Khare (2013) modelled PV–wind–diesel hybrid system with battery storage for a village in Madhya Pradesh. Sharafi *et al*. (2017) found that the best configuration of PV array, wind turbines converter and batteries storage bank to the minimum levelized cost of energy at Yanbu area in Arabia. Chadel *et al*. (2017) presented first, a method to determine the size and optimization of a PV-wind hybrid system for medium power. Secondly, determined the optimum techno economic configuration for the site of Tlemcen. Sorgato *et al.* (2017) analyzed for the first time in Brazil and under current PV module prices, the technical and economic potential of PV modules on a commercial building.

3. METHODOLOGY

The non-residential building discussed in this study is a single-storey building used as a policlinic building and has a total floor area of 200 m^2. The general appearance of the building is given in Fig. 1.

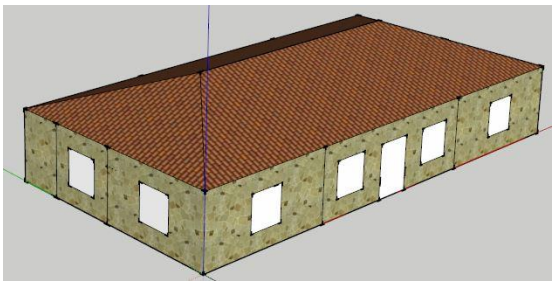

Fig. 1. EnergyPlus model for polyclinic in Mersin

Heating and cooling loads of the policlinic were found using EnergyPlus software.

The coefficient of performance (COP) of the heat pump to be used for heating and cooling the polyclinic is 4.13 and energy efficiency ratio EER is 2.28.

Scheduling of the parameters used to determine energy demand of the polyclinic is done for weekdays between 08.00-17.00.

For the examination of the heating and cooling loads of the polyclinic, the building is divided into 7 zones. Floor plan for polyclinic is given in Fig. 2.

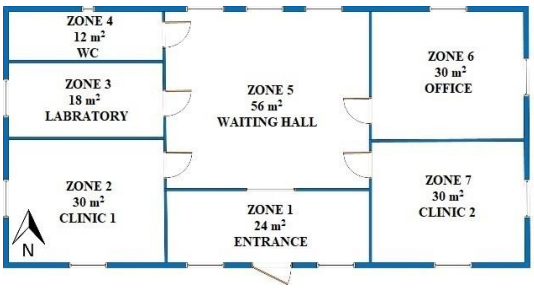

Fig. 2. Floor plan for polyclinic

The structural components of the building are given in table 1.

Table 1. Structural components of the polyclinic

Roof	Tile, 100 mm	Internal wall	Plaster cover plate, 5.9 mm
	Shingle backer, 9.5 mm		Gypsum plate, 19 mm
	Wood, 25 mm		Brick, 100 mm
	Ceiling air space resistance		Insulation board, 50 mm
	Glass wool insulation, 75 mm		Gypsum plate, 19 mm
	Asphalt coating		Plaster cover plate, 5.9 mm
	Lightweight concrete block, 150 mm	Outer wall	Insulation board, 10 mm
Ceiling	Artificial marble, 25 mm		Insulation board, 75 mm
	Cement plaster, 10 mm		Brick, fired clay, 102 mm
	Heavyweight concrete, 100 mm		Wall air space resistance
Window	Clear glass, 3 mm		Gypsum plate, 19 mm
	Air gap, 13 mm	Floor	Artificial marble, 25 mm
	Clear glass, 3 mm		Cement plaster, 10 mm
Door	Wood, 25 mm		Heavyweight concrete, 100 mm

In order to use EnergyPlus software for Mersin, a climate data file with epw extension was needed. This file is available only for İstanbul, İzmir and Ankara in Turkey. Therefore, a climate data file with epw extension was created for Mersin. Dry bulb temperature, relative humidity, atmospheric pressure, wind direction, wind speed and cloudiness rate data required for the software obtained from Turkish State Meteorological Service. Dew point temperature and solar parameters were calculated using the matlab code.

For thermal calculations required lighting power density, human occupancy, heat gain from devices, filtration and infiltration rates, set point temperatures for heating and cooling for each zone are determined according to 55, 62.1 and 90.1 ASHRAE standards. These values are given in Table 2.

Table 2. Design criteria for each zone

Zones	Lighting Power Density (W/m^2)	Human Occupancy (m^2/person)	Heat Gain From Devices (W/m^2)	Ventilation Flow Rate (m^3/s)	Infiltration Rate (m^3/m^2s)	Setpoint Temperature for Heating / Cooling (°C)
1	2	4	15.42	-	0.001	24/26
2	8	5	4.6	0.4	0.001	24/26
3	8	4.5	46	0.37	0.001	24/26
4	5	3	0	0.46	0.001	24/26
5	8	28	17.86	0.5	0.001	24/26
6	8	5	42.27	0.3	0.001	24/26
7	8	5	4.6	0.4	0.001	24/26

In this study, all energy gains or demands were calculated hourly. By using sum of these, daily, monthly and annual values were found.

3.1. Wind Energy Analysis

In this study, the wind data measured at the height of 10 m was obtained from Turkish State Meteorological Service. Wind frequency profile for Mersin, Turkey is illustrated in Fig. 3.

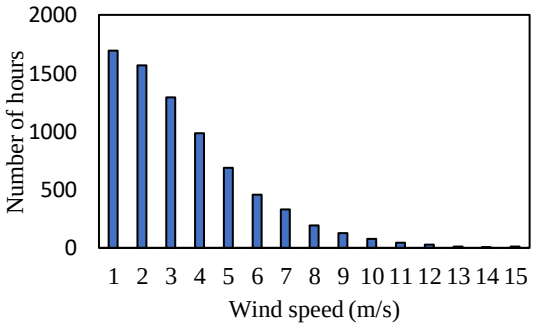

Fig. 3. Wind frequency profile for Mersin, Turkey

About 55 % wind speed in Mersin ranges from 2 m/s to 5 m/s. High-efficiency small wind turbine at 2-5 m/s band for domestic usage is applicable for non-residential buildings.

Fig. 4 illustrates the average, maximum and minimum monthly dry bulb temperature distribution. The annually highest statistic temperature is 39.1 ºC and the lowest statistic temperature is -1.8 ºC. The cooling load of the polyclinic will be higher than the heating load because the Mersin has warm climate.

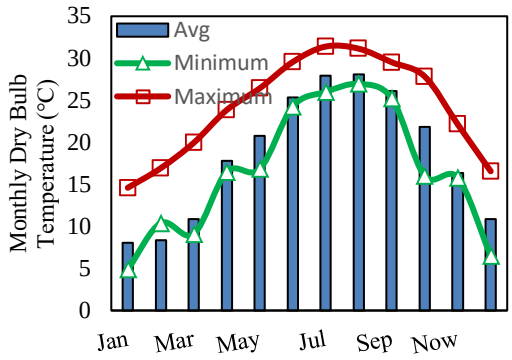

Fig.4. Monthly dry bulb temperature distribution for Mersin, Turkey

There are many distribution functions that are used to determine the distribution of wind speed. Weibull distribution function, which is common in the calculation of wind energy potential, is used in this study. To find the Weibull probability function, two parameters must be known. These are k, shape and c, scale factors. Weibull probability function is calculated from Eq. (1).

$$f(V)=\left(\frac{k}{c}\right)\left(\frac{V}{c}\right)^{k-1}\exp\left(-\left(\frac{V}{c}\right)^{k}\right) \tag{1}$$

The shape factor k and the scale factor c of the Weibull distribution are estimated using Eq. (2) and Eq. (3).

$$k=\left(\frac{\sum_{i=1}^{n}V_i^k\ln(V_i)}{\sum_{i=1}^{n}V_i^k}-\frac{\sum_{i=1}^{n}\ln(V_i)}{n}\right)^{-1} \tag{2}$$

$$c=\left(\frac{1}{n}\sum_{i=1}^{n}V_i^k\right)^{1/k} \tag{3}$$

The average velocity can be written as in Eq. (4) by calculating from the probability distribution function.

$$V_{avg}=c\Gamma\left(1+\frac{1}{k}\right) \tag{4}$$

Where V_i is the wind speed in time step i and n are the number of non-zero wind speed data points.

Actual power generated by wind turbine can be calculated by using Weibull distribution function and parameters. Actual power is defined according to the power curve of the wind turbine. Power curve of the wind turbine is given in Eq. (5).

$$P_T(V)=\begin{cases}0 & V<V_K\\ (a_1V^3+a_2V^2+a_3V+a_4) & V_K\le V<V_R\\ P_R & V_R\le V<V_B\\ 0 & V\ge V_B\end{cases} \tag{5}$$

V_R, V_K, V_B are rated, cut-in and cut-off wind velocities, respectively. Constants defined as a_1, a_2, a_3 and a_4 are obtained by regression analysis of the power curve between V_R and V_K velocities. Actual power generated by wind turbine is obtained by multiplying the produced power at each wind velocity by the Weibull distribution function.

$$E_{TG}=T\int_{V_K}^{V_B}P_T(V)\,f(V)dV \tag{6}$$

$$E_{TG}=T\int_{V_K}^{V_R}(a_1V^3+a_2V^2+a_3V+a_4)\frac{k}{c}\left(\frac{V}{c}\right)^{k-1}e^{-(V/c)^k}dV + TP_R\int_{V_R}^{V_B}\frac{k}{c}\left(\frac{V}{c}\right)^{k-1}e^{-(V/c)^k}dV \tag{7}$$

In that study, wind turbine with capacity 0.9 kW are used. Specifications of the wind turbine is given in Table 3.

Table 3. Specifications of the wind turbine

Rotor Diameter (m)	2.4
Swept Area (m^2)	4.52
Rated Power (kW)	0.9
Cut-in Wind Speed (m/s)	2.3
Rated Wind Speed (m/s)	60

Power curve and generated power equation are obtained according to the fabrication data of the wind turbine and are shown in Fig. 5.

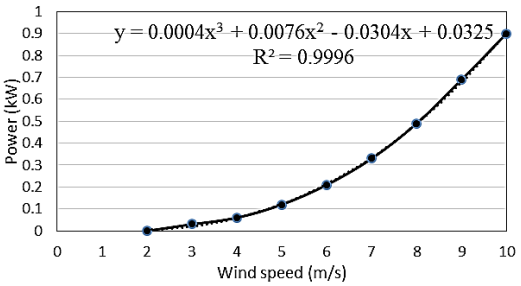

Fig. 5. Power curve and generated power equation

3.2. Solar Energy Analysis

The simplest model given in Eq. 8 for predicting photovoltaic energy production is used in that study.

$$P=A_s.f_a.G_T.\eta_{cell}.\eta_{invert} \tag{8}$$

P is the electrical power produced by photovoltaics, A_s is net area of surface (15 m^2), f_a is the fraction of surface area with active solar cells (0.8), G_T is total solar radiation incident on PV array, η_{cell} is module conversion efficiency (% 20) and η_{invert} is DC to AC conversion efficiency (%95). It is assumed that wind turbine and PV panel are connected to region electricity grid. If electricity generated from wind turbine is not enough for the whole building electricity demand, required amount of energy is obtained from the region electricity grid. Otherwise, excess produced energy is transmitted to the grid.

The correlation given in Eq. (9) is known as the Angstrom equation. Where Q is daily global horizontal solar radiation, Qo is daily extraterrestrial solar radiation, t is sunshine duration and t_o is day length. Constants a and

b are determined by statistical methods based on measurements of all solar radiation and sunshine duration. In this study, Kılıç and Öztürk (1980) model was used. According to this model coefficients a and b are given in Eq. (10) where Z is altitude, e is latitude and d is declination angle.

$$\frac{Q}{Q_o} = a + b\frac{t}{t_o} \tag{9}$$

$$\begin{aligned} a &= 0{,}103 + 0{,}000017Z + 0{,}198\cos(e-d) \\ b &= 0{,}533 - 0{,}165\cos(e-d) \end{aligned} \tag{10}$$

3.3. Cost Analysis

The total cost of the hybrid system consisting of wind and solar energy in non-residential buildings consists of capital cost (C_C), energy cost during operation (C_E) and operating cost (C_O). This relation is given in Eq. (11).

Capital cost includes annual depreciation or amortization cost.

$$C_T = C_C + C_E + C_O \tag{11}$$

The cost of the wind turbine system (I_{WT}) and the cost of the photovoltaic panel system (I_{PV}) are components of the capital cost. This relation is given in Eq. (12).

$$\begin{aligned} C_C &= \left(\frac{1}{n} + \frac{z}{2}\right)\left(I_{WT} + I_{PV}\right) \\ &= \alpha\left(I_{WT} + I_{PV}\right) \end{aligned} \tag{12}$$

Where n is the period of recycling, z is the interest rate and α is refund coefficient. α takes a value ranging from 0.1/year to 0.25/year.

Energy cost during operation (C_E) equal to the energy generated by wind turbine and photovoltaic panels multiplied by unit price of electricity. This value reduces the total cost.

The operating cost (C_O) consists of items such as maintenance, cleaning and repair of the solar and wind energy system and is practically used as in Eq. (13). Where GE is generated energy (MWh) and UOE is unit operating expenses. UOE is 50 TL/MWh for wind turbine, 50 TL/MWh for PV (Zile, M. 2013).

$$C_O = \text{GE } x \text{ UOE} \tag{13}$$

4. RESULTS AND DISCUSSION

4.1. Wind Speed Distribution of Mersin

In this section, the velocity distributions obtained by using hourly wind data measured at a height of 10 m in Mersin station are examined monthly and annually. The annual average wind speed obtained by using 10 m high wind data from Mersin Station is 1.41 m/s. Daily average wind speed exchange rate according to the months is illustrated in Fig. 6. Accordingly, it is understood that the month with the highest average daily wind speed is May and the month with the lowest wind speed is January.

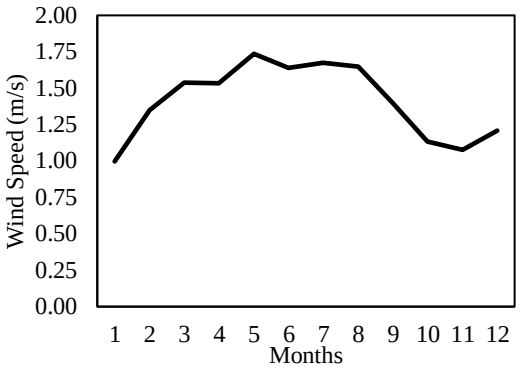

Fig.6. Mersin station average monthly wind speeds

The Weibull probability function for May and January is given in Fig. 7. Accordingly, it is understood that the wind frequency values for high speeds are higher in May than in January. It is also understood that wind speeds in January are 1-2 m/s band, and in May are at 2-4 m/s band.

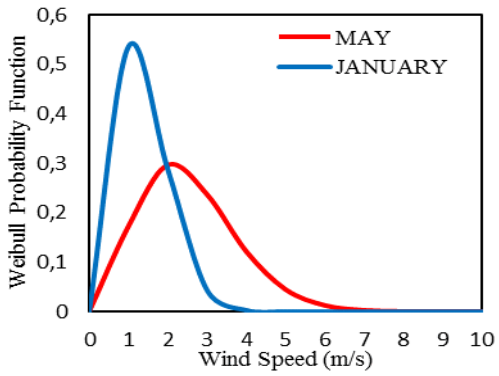

Fig. 7. January and May wind distributions

The annual Weibull probability function is given in Fig. 8. Accordingly, it is understood that the wind speeds are at 1-3 m/s band.

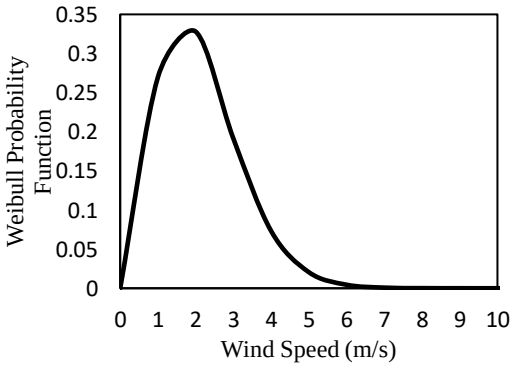

Fig. 8. Annual wind distribution

The Weibull probability function for seasons is given in Fig. 9.

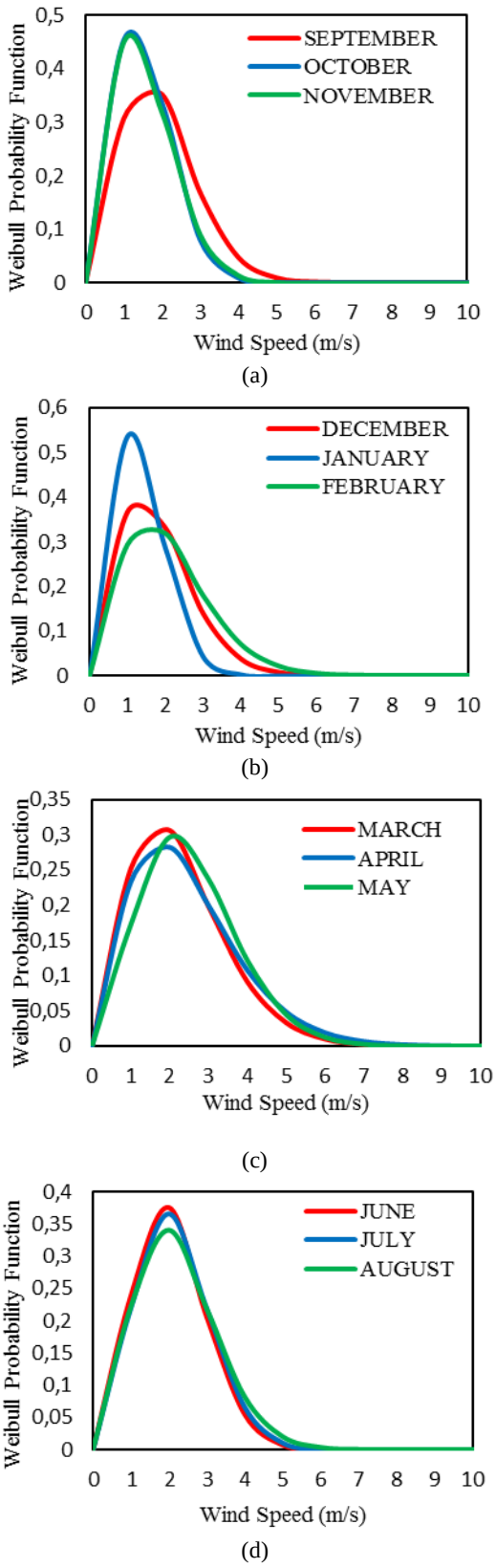

Fig. 9. Seasonal wind distributions; (a) for autumn; (b) for winter; (c) for spring; (d) for summer

4.2. Generated Energy from Wind Turbine

Generated daily energy from the 0.9 kW capacity wind turbine is illustrated in Fig. 10. The total annual energy generation by the wind turbine is 2223.5 kWh and the average daily energy production is 6.1 kWh.

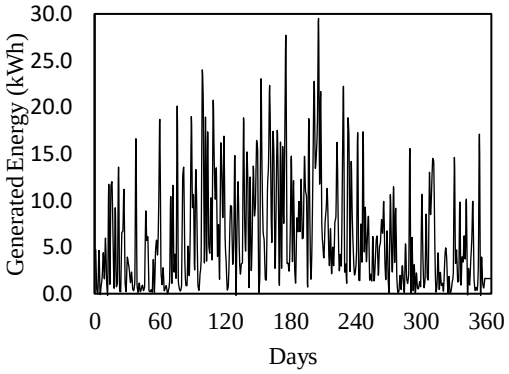

Fig. 10. Daily generated energy from the wind turbine

4.3. Solar Radiation Values

Daily total horizontal plane radiation is given in Fig. 11. Accordingly, Average daily total horizontal radiation is 4642 W/m^2. On summer days this value is up to 7287 W/m^2.

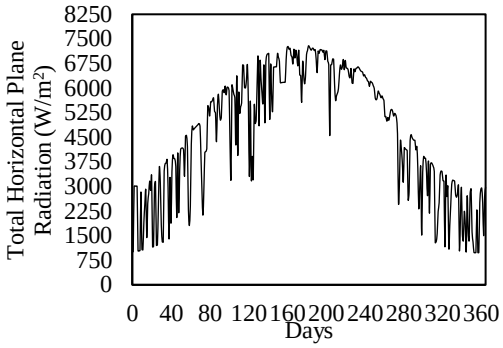

Fig. 11. Daily total horizontal plane radiation

Daily total inclined plane radiation is given in Fig. 12. Accordingly, average daily total inclined plane radiation is 5144 W/m^2. On summer days this value is up to 6697 W/m^2.

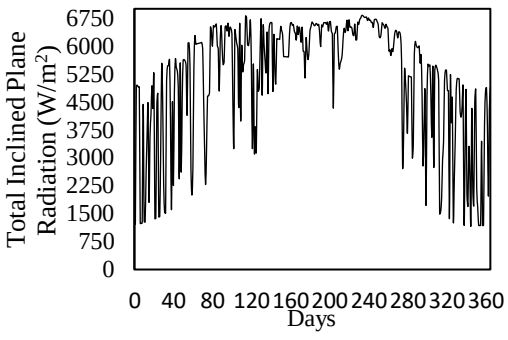

Fig. 12. Daily total inclined plane radiation

4.4. Generated Energy from PV Panels

The daily energy obtained by using 10 pieces of photovoltaic panel with 1.5 m^2 area is given in Fig. 13. A total of 4240 kWh of energy can be generated annually from these photovoltaic panels. The average daily energy production is 11.62 kWh.

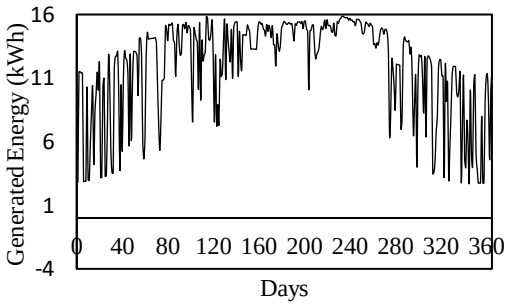

Fig. 13. Daily generated energy from the pv panels

4.5. Amounts of Energy Consumed

The daily heating and cooling loads of polyclinic are given in Fig. 14. The average daily cooling load is approximately 33 kWh on annual basis. Total annual thermal load is 12076.92 kWh.

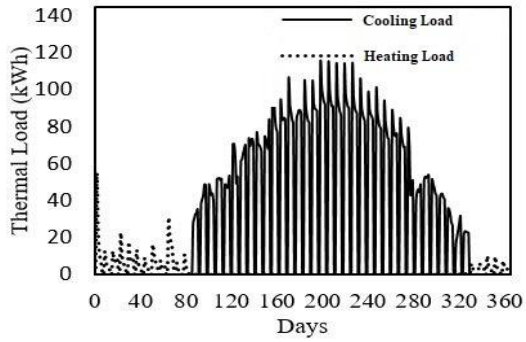

Fig. 14. Heating and cooling loads of the polyclinic

The daily electrical energy consumed by the air-source heat pump to meet the heating and cooling load of the polyclinic is given in Fig.15. Accordingly, consumed energy for cooling is fairly higher than for heating.

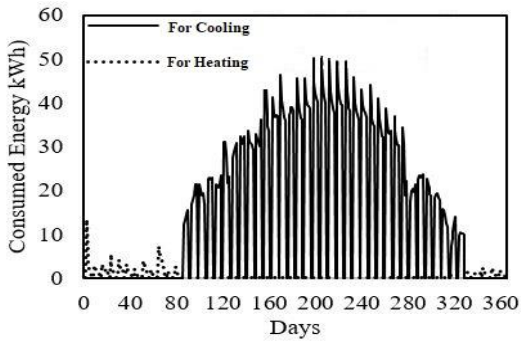

Fig. 15. Air-source heat pump energy consumption

In addition to the heating and cooling loads, the energy consumed by the electrical equipment needs to be taken into account when determining the total energy demand of the non-residential building. The total energy consumed by electrical equipment is 38.44 kWh. The annual total energy consumption is 14030.6 kWh.

Coverage ratio of total daily energy demand from the sum of solar and wind energy is given in Fig. 16.

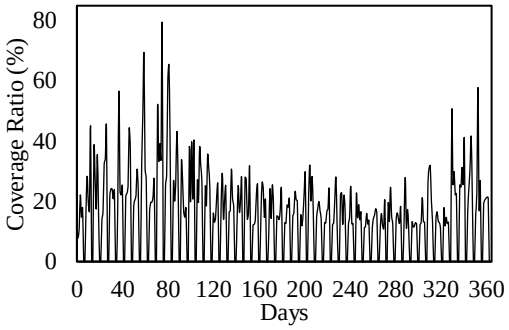

Fig. 16. Coverage rate of daily energy demand

Total consumed energy forms thermal loads and other electrical equipment. Thermal loads are 12076.92 kWh and other electrical equipment constitute annual energy consumption of 14030.6 kWh. Sum of these (26107.52 kWh) represents the annual total energy demand of the polyclinic. 8.51 % of this energy demand is covered by wind turbines and 16.24 % by photovoltaic panels.

4.6. Hybrid System Cost Analysis Results

According to market research, the cost of 15 photovoltaic panels (total power = 5kW) together with the whole system (installation, inverter, battery and connections, etc.) costs 10000 TL. The cost of the 0.9 kW wind turbine with the whole system (installation, battery, charging unit, battery group, inverter, tower etc.) is 6500 TL. Total annual energy production of the solar-wind hybrid system was calculated as 6463.5 kWh. When this value is multiplied by unit price of electricity (0.39 TL/kWh), 2520.76 TL/year profit is obtained. As a result, the lifetime of these two systems is n = 20 years. The depreciation time of the hybrid system that is considered to be established is calculated as 17 years. If the hybrid system did not include a 0.9 kW wind turbine and only solar panels were used, the depreciation time would be reduced to 11 years.

5. CONCLUSION

In this study, a single-floor polyclinic building with a covered area of 200 m^2 located in Mersin was dealt with. In this building, the applicability of wind and solar energy technologies has been investigated. The results of the study are as follows:

- The wind energy potential of the studied region is low. The average annual speed of the Mersin Station using 10 m high wind data is 1.41 m/s. The average daily energy production from the wind turbine is 6.1 kWh.
- The solar energy potential of the region studied is high. The average daily solar radiation from the photovoltaic panel with a slope angle of 30º is 5144 W/m^2.

The average daily energy output from the photovoltaic panels is 11.62 kWh.

- The daily average energy demand of the non-residential building is 35 kWh.
- 8.51 % of the annual energy requirement of the non-residential building is covered by wind turbines and 16.24 % by photovoltaic panels.
- The hybrid system, which consists of wind and solar energy, has a depreciation of 17 years. It is not applicable to use this system in the non-residential building since the system lifecycle is 20 years.
- If only the photovoltaic panel system is used, the depreciation time will be reduced to 11 years and a similar system is applicable.

ACKNOWLEDGEMENTS

This study was supported by the Research Fund of Mersin University in Turkey with Project Number: BAP-FBE MMB (BB) 2013-4 YL.

REFERENCES

Al-Sharafi, A., Sahin, A. Z., Ayar, T. and Yilbas, B. S. (2017). "Techno-economic analysis and optimization of solar and wind energy systems for power generation and hydrogen production in Saudi Arabia." *Renew Sustain Energy Rev*, Vol. 69, pp. 33-49

ANSI/ASHRAE Standard 55 (2004). *Thermal Environmental Conditions for Human Occupancy.*

ANSI/ASHRAE Standard 62.1 (2007). *Ventilation for Acceptable Indoor Air Quality.*

ANSI/ASHRAE Standard 90.1 (2007). *Lighting Power Densities.*

ASHRAE (2009). *Handbook-Fundamentals (SI).*

World Energy Council, Turkish National Committee (WECTNC) Energy Report, (2002).

Bekele, G. Boneya, G. (2012). "Design of a photovoltaic–wind hybrid power generation system for Ethiopian remote area." *Energy Procedia*, Vol. 14, pp. 1760–1765.

Belmili, H. Haddadi, M. Bacha, S. Almi, M. F. and Bendib, B. (2014). "Sizing stand-alone photovoltaic–wind hybrid system: techno-economic analysis and optimization." *Renew Sustain Energy Rev*, Vol. 30, pp. 821–832.

Chadel, A., Chadel, M., Aillerie, M. and Benyoucef, B. (2017). "Technical and economic analysis of hybrid solar/wind energy source for the site of Tlemcen-Algeria." *Energy Procedia*, Vol. 119, pp. 29-37.

Dalwadi, P. G and Mehta, C. R. (2012). "Feasibility study of solar–wind hybrid power system." I*nt J Emer Technol Adv Eng*, Vol. 2, pp. 125–128.

Essalaimeh, S., Al-Salaymeh, A. and Abdullat, Y. (2013). "Electrical production for domestic and industrial applications using hybrid PV–wind system." *Energy Convers Manage*, Vol. 65, pp. 736–743.

Hoque, M. M., Bhuiyan, I. K. A., Ahmed, R., Farooque, A. A. and Aditya, S. K. (2012). "Design, analysis and performance study of a hybrid PV–diesel–wind system for a village Goplal Nagar in Comilla." *Global J Sci Frontier Res Phys Space Sci*, Vol. 12, pp. 13–17.

Islam, A. K. M. S., Rahman, M. M., Mondal, M. A. H. and Alam, F. (2012). "Hybrid energy system for St. Martin Island, Bangladesh: an optimized model." *Procedia Eng*, Vol. 49, pp. 179–188.

Ioannis, P., Panapakidis, N., Dimitrios, Sarafianos, Minas, C. and Alexiadis. (2012). "Comparative analysis of different grid-independent hybrid power generation systems for a residential load." *Renew Sustain Energy Rev*, Vol. 16, pp. 551-563.

Lal, S. and Raturi, A. (2012). "Techno-economic analysis of a hybrid mini-grid system for Fiji islands." *Int J Energy Environ Eng*, Vol. 3, pp. 1–10.

Meherchandani, J. K., Agarwal, C. and Sahi, M. (2012). "Economic feasibility of hybrid biomass-PV-wind system for remote villages using HOMER." *Int J Adv Res Electr, Electron Instrum Eng*, Vol. 1, pp. 49–53.

Sorgato, M. J., Schneider, K. and Rüther, R. (2017). "Technical and economic evaluation of thin-film CdTe building-integrated photovoltaics (BIPV) replacing façade and rooftop materials in office buildings in a warm and sunny climate.", *Renewable Energy*, doi: 10.1016/j. renene.2017.10.091.

Vani, N. and Khare, V. (2013). "Rural electrification system based on hybrid energy system model optimization using HOMER." *Can J Basic Appl Sci* 2013;1:19–25.

Zile, M. (2013). ''Integration of Solar and Wind Power Plants into Smart Grids for Tarsus District'' Proc., Akıllı Şebekeler ve Türkiye Elektrik Şebekesinin Geleceği Sempozyumu, Ankara, Turkey.

Turkish Journal of Engineering

Turkish Journal of Engineering (TUJE)
Vol. 2, Issue 1, pp. 35-37, January 2018
ISSN 2587-1366, Turkey
DOI: 10.31127/tuje.341617
Research Article

MEASURES TO BE DETERMINED AND RECEIVED IN UNIVERSITIES OF OCCUPATIONAL HEALTH AND SAFETY RISKS

Mehmet Zile *[1]

[1] Mersin University, Erdemli Applied Technology and Business School, Department of Information Systems and Information Technology, Mersin, Turkey
ORCID ID 0000 – 0002 – 0457 – 2124
mehmetzile@yahoo.com

* Corresponding Author
Received: 04/10/2017 Accepted: 12/11/2017

ABSTRACT
Occupational health and safety related to the work done in workplaces in general people full body health and safety provision. In our country, the occupational health and safety risk assessment analysis moral, legal, and indirect costs have become crucial. Located in the workplace or identification of hazards from outside intrusion, it turned into a risk of danger that led to the factors analyzed by ranking of the risks arising from the dangers with and control measures will be utilized for the purposes of risk assessment and analysis work required. The work done in the business risks, in-flight transactions are used various methods, materials, and all kinds of machinery and equipment, job location or in the vicinity of the workplace are environmental conditions and various organizations created elements interact with each other. In this study, the University occupational health and safety measures to be taken by determining risks that are emphasized.

Keywords: *OHS at The University, Determination of Risk at Universities*

1. INTRODUCTION

In parallel with technological developments in the world and in our country, especially in the workplace, the best healthy environment should be presented. The employees should be protected from the negative effects of the working conditions. The best possible harmony between the worker and the worker should be obtained. The risks in the workplace should be completely removed or the damage should be minimized. Material and moral damages must be removed. Possible hazards in the workplace; use of mobile hand tools, use of stationary machines and benches, ladders-platforms with mobile access, mechanical, electrical and electronic equipment, thermal comfort conditions (temperature, humidity, ventilation), chemical factors (toxic gases and vapors, organic solvents), fire and explosion, hand transportation, electrical appliances, pressure vessels, inadequate lighting, and dusts), biological agents (microorganisms, bacteria, viruses) and routine work. Some of these hazards are unsafe actions, while others are unsafe conditions. In this study, the health and safety risks of the university are determined and the precautions to be taken are emphasized. (Labor Law No. 6331)

2. MEASURES TO BE DETERMINED AND RECEIVED IN UNIVERSITIES OF OCCUPATIONAL HEALTH AND SAFETY RISKS

In college study offices, there is a possibility that there are deformations that may cause slipping or falling of the floor, glass surfaces are mounted properly. Shelves are mounted on the walls in the office, monitors and other materials are fixed firmly, furniture used in the office is regularly checked, whether all areas in the office are regularly ventilated, whether the temperature and humidity in the office are uncomfortable, whether it is sufficient to illuminate the work area, whether it is reserved for tea, coffee, eating and drinking activities. The layout is designed so as not to restrict the activities of the employees. It is arranged in such a way as to prevent hanging or falling off of the wired instruments used in the office. All fuses and power panels must be insulated in protective cabinets. Electrical fuse boxes must be locked, a limited number of switches must be made to prevent unauthorized access. There must be an open wire, and the integrity of the plugs should be checked regularly (Labor Law No. 6331). Electrical equipment is checked regularly, fire escape doors/emergency exits are open at any time. Fire escape doors/emergency exit doors are opened out. Fire escape doors/emergency signs indicating escape routes are placed in appropriate places. Lighting of doors and escape routes, presence or absence of fire extinguishers, emergency telephone numbers in the office are visible in the Office. It is important that employees are provided with appropriate tables, chairs or supporting equipment for the work. They are doing, a first aid cup with sufficient material inside: Employees are trained and directed on the work they are doing, urgent matters must be fulfilled. Hazards encountered in universities are not due to leakage current relay, panel doors are open. There are no insulating materials in front of the panels. Electrical outlets are not suitable, electrical cables and connections are not suitable, danger caused by exposed cables, danger caused by worn crushed electrical cables. The use of keyboards, ergonomics of seating seats, injuries caused by improper stacking of materials, no precautions taken to prevent sliding of the area to be cleaned, hazards posed by chemicals used in cleaning works, loads not suitable for the physical structure of employees, heavy and heavy loads it can be said to be the danger posed by not being properly loaded. In case of fire, there are not enough fire extinguishers, no pre-fire exercises, no fire exit directions and signs, students cannot be safely evacuated in case of fire. Emergency telephone numbers are not visible at the entrance of the building, fire escape doors are locked the absence of security devices at the entrance door, the lack of safety gates, the lack of sufficient safety cameras, the lack of safety equipment and instructions for use in electrical appliances, the lack of grounding control, the uncontrolled use of the mincing machine, failure of natural gas connection pipe, inadequate ventilation, lack of general hygiene, the absence of lift elevator emergency cessation, the running of students and the use of the emergency room, the failure to open the door of the refrigerator, the absence of the lift maintenance instructions, the absence of instructions to use the elevator, the interruption to unauthorized persons, the lack of awareness of the speed limits of the vehicles at school, the rushing of the students while the vehicles are moving, the failure of the drivers to obey the traffic rules of the university, the service vehicles without periodic maintenance, the general job health and safety training for the university employees and the danger that the employees are not trained and directed about the work that can be expressed (Zile, 2013). In Fig. 1, a model of causality in job accidents was created to prevent work accidents at universities.

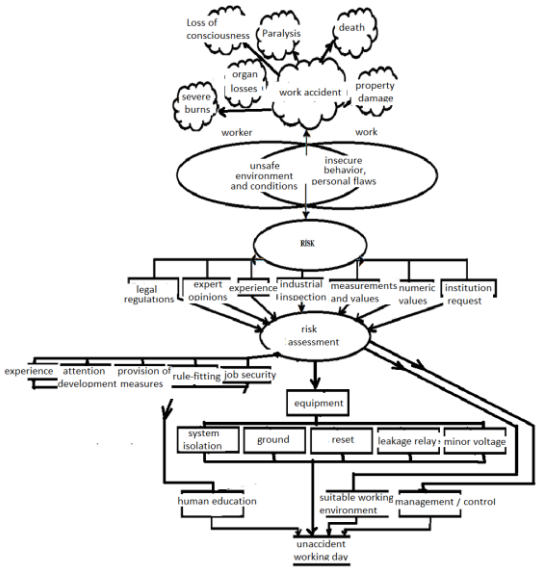

Fig. 1. Model of causality in job accidents was created to prevent work accidents at universities

Human education / Business method; In order to prevent work accidents at universities, university personnel should be trained at certain periods in both

occupational and occupational safety areas. The new starting staff should never be employed without training in the work and job security areas they are working on. Personal protective equipment such as helmets, goggles, shields and masks must be used when personnel work on workers' machines. Do not overload with lift trucks and do not stack over 2.5 meters of material. Materials should be labeled and necessary warnings. Warnings should be written. It should be observed whether there is a malfunction in the starting and ending machines. The machines must not be suddenly loaded without giving way and the idle operation should not be stopped unexpectedly. If electrical energy is required, maintenance and repair should not be carried out on the machine without being cut off from two places, and a power button should be taken against the key or unexpected movement during maintenance and repair. Repairs and welding should not be done until the warehouse and containers are completely emptied and cleaned. Smoking areas are strictly non-smoking. Loading and unloading operations must be carried out in a convenient and convenient manner. Ungrounded machines and hand tools should not be used, groundings should be checked at regular intervals. Older electrical installations in workplaces should be renovated and maintained at regular intervals. Unauthorized access to the workplace should not be allowed. When working with high voltage the floor must be insulated and the written instructions and rules must be observed. (Zile, 2013)

Working Environment; In universities, the floor should not be slippery, there should be external amenity gates and exits from each section, the working area should be adequate and regular, the stairs must have railing, showers and toilets should be clean and working, vibration, noise, radiation, infrared and ultraviolet rays toxic gases, liquid vapors and metal gases should not leach into the working environment, should not leach into the working environment, acids and bases in combustion, inert dusts, fibrogenic dusts, toxic dusts, carcinogenic dusts and allergic dusts. The tool must be cleaned after the machine and machine work is finished and the tools should be placed back in place. Avoid contamination of the workplace area and the environment should be kept clean with cleaning materials such as detergent, special medication as much as possible on the workplace. Business waste and garbage should be collected and removed from work environment. Oil, diesel etc. that may cause slipping. Petroleum products should be cleaned immediately. Those who do not comply with cleaning and ordering rules should be warned. (Zile, 2013)

Machinery Hardware; Machines and materials in university workshops should be placed in convenient and safe locations. Machines must have oppressive, piercing, cutting, rotating operation guard, two-hand control on the presses, and foot pedal guard. The guard of the transmission belts must be fitted. The machines must have an energy-off button or isolator to stop abruptly in the event of a hazard. Old and frequently malfunctioning machinery and protective materials should not be used and should be replaced immediately. The warning systems must be technologically sufficient, the maintenance and periodic checks of the machines, lifting appliances, boilers, compressors must be carried out on time. (Zile, 2013)

Management/Control; The university management should establish conditions appropriate to the characteristics of the works being carried out, periodically train the staff on occupational and occupational safety issues, and fulfill the obligations imposed on them by the legislation against labor and environment. (Zile, 2013)

5. CONCLUSION

In the formation of business accidents, production technology, production tools, environmental conditions, as well as many sociological, psychological, physiological factors play a role. However, all of the factors that cause job accidents can be reduced by two basic factors. These are the insecure situations in the university and the insecure behavior of employees. In this study, the measures to be taken by determining the occupational health and safety risks in university are emphasized and it is observed that the risks in universities are decreased when these measures are taken.

REFERENCES

Labor Law No. 6331

Regulations Regarding the Law No. 6331

Zile, M., "Analysis of Work Accidents Transmitted to the Jury and Formation of Causality Model" VII. National Occupational Health and Safety Congress, Publication No: E/2013/600, 295-298, Çukurova University, Adana, 2013.

Zile, M., "Occupational Approaches to Occupational Accidents Due to Electricity Energy and Formation of Occupational Safety", VII. National Occupational Health and Safety Congress, Publication No:E/2013/600, 295-300, Çukurova University, Adana, 2013.

CONTENTS

CHARACTERIZATION OF HYDROTHERMALLY SYNTHESISED HYDROXYAPATITE BIOCERAMIC
Canan Aksu Canbay, Himdad İbrahim Mustafa and İskender Özkul.....1

AGING EFFECTS ON TRANSFORMATION TEMPERATURES AND ENTHALPIES FOR TiNi ALLOY
Canan Aksu Canbay and İskender Özkul.....7

THE EFFECT OF SODIUM CARBONATE ON ELEVATED TEMPERATURE RESISTANCE OF CEMENT MORTARS CONTAINING NATURAL ZEOLITE
Cahit Bilim.....12

LIGHTWEIGHT FOAM IMPACT ATTENUATOR DESIGN FOR FORMULA SAE CAR
Emre İsa Albak, Erol Solmaz, Necmettin Kaya and Ferruh Öztürk.....17

GALVANIC CORROSION OF ZINC ANODE AND COPPER CATHODE CELL
Nurettin Çek.....22

APPLICABILITY OF SOLAR AND WIND ENERGY TECHNOLOGIES FOR A NON-RESIDENTIAL BUILDING
Burhan Bayhan and Gökhan Arslan.....27

MEASURES TO BE DETERMINED AND RECEIVED IN UNIVERSITIES OF OCCUPATIONAL HEALTH AND SAFETY RISKS
Mehmet Zile.....35

ISSN 2587-1366

TURKISH JOURNAL OF ENGINEERING

VOLUME 2 ISSUE 1 JANUARY 2018